Basal channels, ice thinning and grounding zone retreat at Thwaites Glacier, West Antarctica

Allison M. Chartrand[1,2], Ian M. Howat[3], Ian R. Joughin[4], Benjamin Smith[4]

[1]Earth System Science Interdisciplinary Center, University of Maryland, College Park, MD, USA
5 [2]NASA Goddard Space Flight Center, Greenbelt, MD, USA
[3]Byrd Polar and Climate Research Center, Ohio State University, Columbus, OH, USA
[4]Applied Physics Laboratory, University of Washington, Seattle, WA, USA

Correspondence to: Allison M. Chartrand (allisonchartrand@gmail.com)

Abstract. Antarctic ice shelves buttress the flow of the ice sheet, tempering sea level rise, but they are vulnerable to basal
10 melting from contact with the ocean, as well as mass loss due to fracture and calving. Melt channels and similar features at the
bases of ice shelves have been linked to enhanced basal melting and observed to intersect the grounding line, where the greatest
melt rates are often observed. The ice shelf of Thwaites Glacier is especially vulnerable to melt and subsequent retreat of the
grounding line because the glacier has an inland–sloping bed leading to a deep trough below the grounded ice sheet. We use
digital surface models from 2010–2022 to investigate the evolution of ice–shelf basal channels and a proxy for the grounding
15 line on the Thwaites Glacier ice shelf. We find that the highest sustained rates of grounding–line retreat (up to 0.7 km a^{-1}) are
associated with high melt rates (up to ~250 m a^{-1}) near the intersections of basal channels with the grounding zone, steep local
retrograde slopes, and where subglacial channel discharge is expected. Detailed observations of basal channels collocated with
regions of grounding–line retreat will further elucidate the complicated processes occurring at the ice–ocean interface and
hopefully lead to more accurate estimates of current and future ice–shelf melting and evolution.

20 **1 Introduction**

Thwaites Glacier in the Amundsen Sea region of West Antarctica has the potential to contribute up to 65 cm of sea–level rise
(Rignot et al., 2019; Morlighem et al., 2020) and has experienced recent speed–up, ice shelf break–up, thinning, and
grounding–line retreat (e.g. dos Santos et al., 2021). The glacier lies atop an inland–sloping (retrograde) bed leading to a deep
trough reaching 1.5 km below sea level (Morlighem et al., 2020). Several studies have suggested that the Thwaites Glacier
25 grounding zone (GZ, the region where the ice transitions from grounded to freely floating), may already be undergoing rapid,
unstable retreat (Joughin et al., 2014; Goldberg et al., 2015; Rignot et al., 2014; Yu et al., 2018), in a process known as "marine
ice sheet instability", or MISI (Gudmundsson et al., 2012; Schoof, 2007; Weertman, 1974). Much of the melting and retreat is

attributed to enhanced ocean melting (Bevan et al., 2021; Schmidt et al., 2023; Holland et al., 2023) and loss of basal traction upstream of the GZ (Joughin et al., 2024).

30   Several studies have shown that high rates of ice–shelf thinning and melting are often associated with ice–shelf basal channels, which are curvilinear incisions at the ice–shelf base believed to be maintained by buoyant meltwater plumes entrained within them along–flow (Alley et al., 2016; Drews, 2015; Chartrand and Howat, 2020; Gourmelen et al., 2017; Wearing et al., 2021) Others have shown that basal channels are also commonly associated with ice–shelf weakening through fracturing as a result of thinning (Vaughan et al., 2012; Dow et al., 2018; Alley et al., 2019). Basal channels initiate at the

35 grounding line and extend seaward. They often represent advected extensions of subglacial channelization beneath the grounded ice or may be incised by undulations in the bed (e.g. Le Brocq et al., 2013; Alley et al., 2016; Drews et al., 2017). Where they represent extensions of subglacial channels, they are likely formed by a meltwater plume, enhanced by the fresh glacial outflow (Jenkins, 2011). The Thwaites Glacier Ice Shelf (TGIS) has at least four previously mapped basal channels (Alley et al., 2016) and the grounded ice is underlain by at least two persistent subglacial channels intersecting the GZ (Hager

40 et al., 2022). Recently, subglacial channels and aligned basal channels on Greenland ice tongues have been linked to thinning and retreat of the grounding line (Ciracì et al., 2023; Narkevic et al., 2023). It is unknown, however, the extent to which basal channels on the TGIS and/or subglacial channels within grounded ice may have contributed to the thinning and retreat at Thwaites Glacier.

        In the absence of a method for directly measuring ice thickness from space, observations of basal channels and
45 channel–like features (i.e. basal incisions oriented predominantly along–flow without clear evidence of subglacial initiation or entrained meltwater flow) and their relationship to variations in GZ position and other ice–shelf structures are only available from precise measurements of surface height. While relatively frequent and accurate, observations from spaceborne altimetry, such as ICESat and ICESat–2, are limited to ground tracks. Recently, high–resolution digital surface models (DSMs) produced from stereoscopic satellite imagery, combined with altimetry, have been used to map changes in basal channels and other ice–

50 shelf structures (Chartrand and Howat, 2020; Shean et al., 2019; Zinck et al., 2023). Using the extensive collection of repeat DSMs provided by the Reference Elevation Model of Antarctica (REMA) project (Howat et al., 2019), we map the positions of surface depressions overlying basal channels on the TGIS and subglacial channels within grounded ice as well as the landward extent of the transition to flotation as a proxy for the grounding line, termed the hydrostatic boundary (HB). We also construct the most comprehensive maps to date of time–evolving surface height, thickness, and basal mass change for the

55 Thwaites Glacier and TGIS. Here we examine the transient locations of the basal channels relative to those of the HB, as well as to variations in basal melt and flow speed, to assess the potential relationship between channels and grounding–line retreat.

2 Datasets

We use several geophysical datasets for this study as described throughout this section.

2.1 REMA Digital Surface Model (DSM) strips and annual mosaics

60 Reference Elevation Model of Antarctica DSMs for the TGIS are obtained through stereophotogrammetry applied to pairs of commercial submeter–resolution, panchromatic satellite images acquired by the MAXAR constellation, including Worldview–1, –2 and –3, Quickbird–1 and –2, and GeoEye satellites (Howat et al., 2019). Elevations from REMA DSMs are relative to the WGS84 ellipsoid and are distributed both as individual "strips" representing WGS84–ellipsoid elevations, created from a single pair of images along their overlapping swath, and as seamless, continuous mosaics made from those strips. Both product

65 types are distributed at 2 m resolution, with downsampled versions available. We use the REMA 200 m mosaic for the Thwaites region as a base map in several figures.

We utilise the DSM strips at 10 m resolution to map the HB (Section 3.1) and basal channels (Section 3.2). After removing strips with insufficient coverage or low internal quality, as indicated in the metadata by a root–mean–squared error value greater than 1 m, there are 191 strips for the TGIS.

70 We combine REMA strips into full–coverage (depending on strip availability) annual mosaics at 50 m resolution to compute rates of change across the TGIS (Section 3.3). As strips are more readily available for summer months, REMA strips from November to March are mosaicked to form an austral annual mosaic, for which we assign a nominal date of January 1. For each annual mosaic, each strip is co–registered to every other using the method of Nuth and Kaab (2011). The co–registered strips are then stacked, and the annual mosaic is the median height at each pixel through the stack (Fig. S1).

75 As part of this process, each strip and annual mosaic is registered to correct for single–value elevation biases using ICESat–2, CryoSat–2, or Operation IceBridge (henceforth, IceBridge) altimetry data, depending on availability and/or which dataset is temporally closest to the collection date of the strip. The registration dataset selected is based on a hierarchy; if the first dataset is unavailable, the next dataset will be used, and so on. Priority is given to overlapping ICESat–2 ATL06 Version 5 (Smith et al., 2021) or Version 6 (Smith et al., 2023) ground control points (GCPs) that were collected within 10 days of the

80 strip or 100 days of the annual mosaic nominal date, then to GCPs from the ICEBridge Airborne Topographic Mapper (ATM) L1B (Studinger, 2013), the IceBridge Land, Vegetation, and Ice Sensor (LVIS) L2 (Blair and Hofton, 2015), or the IceBridge and ICECAP Riegl Laser Altimeter L2 (Blankenship et al., 2012) datasets collected within 10 or 100 days. Strips with no contemporaneous ICESat–2 or IceBridge GCPs were registered to CryoSat–2 SAR–In mode elevations (European Space Agency, 2023) collected within about 365 days of the strip. Unlike ICESat–2 and IceBridge registrations which register the

85 strip to temporally proximal GCPs, the CryoSat–2 registration is determined by a linear fit to elevation differences with respect to time so that the DSM is fit to a temporal model of the elevation data. Strips that do not meet these registration criteria are eliminated, leaving 177 strips over the TGIS (Fig. S2).

The strips and annual mosaics are not smoothed, but they are masked to remove artefacts and errors like clouds. Following registration, the absolute residual, and mean and standard deviation thereof, between each DSM and the REMA

90 mosaic is computed. Then, the residual is smoothed by a 50 pixel (500 m for strips or 2500 m for annual mosaics) moving mean, and any DSM pixels that correspond to a smoothed residual that is 2–5 standard deviations greater than the mean residual

are masked out; a larger magnitude in the residual mean or standard deviation triggers a smaller standard deviation threshold for that strip. These thresholds were chosen to effectively remove artefacts and errors like clouds, but to maintain differences due to the advection of surface features.

95   Following the procedure in Chartrand and Howat (2020), registered and masked strip and annual mosaic ellipsoid elevations are converted to freeboard heights (h) by referencing to mean sea level using the EIGEN–6C4 geoid model (Förste et al., 2014), correcting for Mean Dynamic Topography using the DTU22 MDT model (Knudsen et al., 2021), and correcting for tidal variations using the CATS2008b inverse tide model (Padman et al., 2018).

2.2 BedMachine Antarctica

100   Bed heights referenced to the geoid are obtained from BedMachine Antarctica, Version 3 (Morlighem, 2022). The BedMachine bed heights and thicknesses are used to estimate subglacial conditions (Section 3.4). This dataset also contains masks for floating ice, grounded ice, ice–free land, and ocean which are used to select strips based on their overlapping area with the relevant masks.

2.3 Ice velocities

105   Ice surface velocity for the TGIS is obtained from NASA Making Earth System Data Records for Use in Research Environments (MEaSUREs) mosaicked, 450 m resolution, InSAR–Based Antarctic Ice Velocity Map, Version 2 (Mouginot et al., 2012; Rignot et al., 2011, 2017), the MEaSUREs 1 km posting, SAR–based Annual Antarctic Ice Velocity Maps, Version 1 (Mouginot et al., 2017a), and 250 m posting quarterly velocities that we derived using speckle tracking applied to Sentinel 1 A/B images from TGIS and Pine Island Glacier. The 450 m posting MEaSUREs mosaic is used to obtain masks for ice moving < 20 m a^{-1} for registering strips and for filtering the annual and quarterly velocity maps. The MEaSUREs annual velocity maps obtained for 2011–2015 are variable in their spatial coverage and quality, so for each year we take the median of the annual map and the average velocity map. The quarterly velocity maps obtained for 2016–2023 have more consistent coverage and better quality. For consistency in temporal resolution throughout the study period, we take the median of the two austral summer quarters for each year. These maps are bilinearly interpolated to the same grid as the annual REMA mosaics and further filtered by taking the median velocity and standard deviation at each pixel throughout the time period and masking out pixels in each year where the velocity differs from the median pixel velocity by more than 2.5x the standard deviation for that pixel, then smoothing the velocity for each year with a 600 m moving mean window. The annual velocity maps are used to flow–shift the annual DSM mosaics to obtain Lagrangian rates of change and to investigate changes in velocity where we observe rapid grounding–line retreat.

2.4 Historical grounding lines and calving front

Historical grounding lines are obtained from the MEaSUREs Antarctic Grounding Line from Differential Satellite Radar Interferometry, Version 2 for 7 February 1992 to 17 December 2014 (Rignot et al., 2016). Furthermore, the MEaSUREs

Antarctic Boundaries for the 2007–2009 International Polar Year (IPY) from Satellite Radar, Version 2 dataset (Mouginot et al., 2017b) is also used to obtain a complete and continuous grounding line (henceforth termed 07–09 IPY GL or simply IPY
125 GL).

3 Methods

We use a variety of previously defined and novel techniques to investigate changes on the TGIS, described below.

3.1 Mapping the hydrostatic boundary

The hydrostatic boundary (HB) is defined as the point at which the grounding thickness matches the flotation thickness. The
130 grounding thickness is the distance between the observed ice surface and the bed from BedMachine. Flotation thickness (H_E) is determined from the DSM strip freeboard heights (h) as in Chartrand & Howat (2020, 2023):

$$H_E = h \frac{\rho_s}{\rho_s - \rho_i} - H_a \frac{\rho_a - \rho_i}{\rho_i - \rho_s} \tag{1},$$

where ρ_s is seawater density (1,027 kg m^{-3}), ρ_i is meteoric ice density (918 kg m^{-3}), ρ_a is the firn–air column density (2 kg m^{-3}), and H_a is the thickness of the firn–air column within the freeboard (specifically, the length of the change in firn thickness
135 resulting from compressing the firn column to ice density (Ligtenberg et al., 2011)). The subscript E denotes that H_E is an estimate of ice thickness.

We use the 07–09 IPY GL as the basis for where HBs are expected to be mapped. We track HBs at each independent, continuous grounding line from the IPY, including the continental grounding line and six pinning points (PP1–6). For each strip, the difference between H_E and the grounding thickness is computed at each pixel. This difference is converted to a
140 contour map, and the coordinates of pixels that lie on the 0 m contours are stored as features representing HBs near the continuous IPY GL and each pinning point. These features are filtered and simplified for analysis as follows (Fig. S3). For each strip, HB features containing fewer than 25 coordinates are removed, and the remaining HB feature coordinates are smoothed by a 50 point moving mean (a distance of about 200 m). If the strip has coverage over a given grounding line, a polygon is manually defined to encapsulate the HB features that most likely represent that grounding line (i.e., the polygon is
145 defined to keep the longest and most continuous HB features and eliminate small isolated HBs), and points outside of the polygon are eliminated. Then, HB features are combined by year, and an annual HB with a nominal date of January 1 is manually defined along the most upstream features for the continental GL, and the innermost features for each pinning point, from each year. The annual HBs and unfiltered HB features are shown as curves with a purple–orange–yellow colour scale throughout the figures.

150
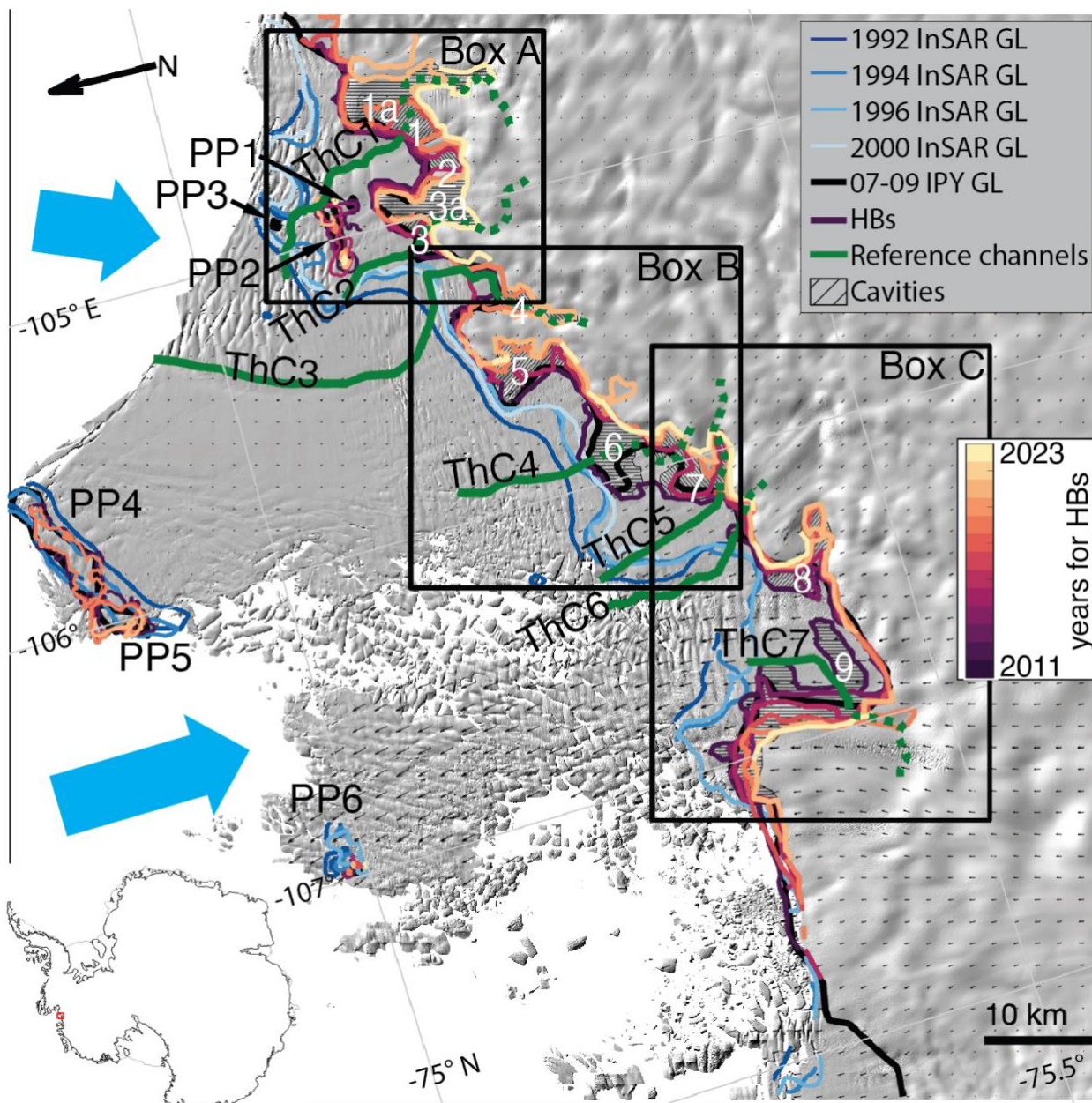
Figure 1: REMA 200 m mosaic hillshade for the Thwaites Glacier and Thwaites Glacier ice shelf (TGIS) overlain by historical grounding lines derived from InSAR (curves in shades of blue), the continuous InSAR–derived 07–09 IPY GL (black curve, including pinning points PP1–6), and selected hydrostatic boundaries (HBs) identified in this study (curves in shades of purple, orange, and yellow, with lighter shades representing more recent HBs). The reference channels for the basal channels and surface depressions identified in this study are shown as solid and dashed green curves, respectively, and labelled ThC1–7. Hatched regions indicate cavities that opened as the HB retreated throughout the study period, labelled 1–9. Large blue arrows indicate the general location of circumpolar deep water (CDW) influx to the ice–shelf cavity (Dutrieux et al., 2014). The black boxes, Box A–C, indicate the zoomed regions in following figures. Small black arrows represent ice flow.

155

160

3.2 Mapping basal channels and surface depressions

Complementary methods are used to locate persistent curvilinear ice–shelf basal features, including basal channels, as they are not directly observable using surface elevation alone. Sufficiently large basal channels (usually > 1 km wide) correspond to surface depressions that are resolvable as stream–like features in the surface topography (Drews, 2015). We do not attempt to
165 verify the presence of entrained meltwater flow in the basal features we identify, and refer to all consistently mapped basal incisions that are oriented predominantly parallel to flow and associated with surface depressions as basal channels. Basal channel locations from Alley et al. (2016) are used to initially query REMA DSM strips.

We map surface depressions over both grounded and floating ice by refining the method of using DSM local minima to map surface depressions (Chartrand and Howat, 2020). We compute maps of hypothetical stream channel depth for the ice–
170 shelf surface from strip freeboard heights using the flow accumulation ("flowacc") function from the MATLAB–based TopoToolbox software (TopoToolbox, 2023). We assume that features with high flow accumulation are surface depressions. We then compare potential depressions with DSM hill shade renderings, eliminating those that align with clear fractures (usually perpendicular to flow), are very short (< ~1 km), or do not intersect the ice shelf.

To identify basal channels on the shelf, we compute flotation thickness from strip freeboard height (Eq. 1) and
175 determine the depth of the hydrostatic ice–shelf draft ($h - H_E$) relative to sea level. We invert the ice–shelf draft by multiplying its depth by -1, and again compute the hypothetical stream channel depth and flow accumulation across the inverted ice–shelf base, with the locations of stream flow identified as possible basal channels. As for the surface depressions, we remove spurious features by comparison with DSM hill shade renderings of both the surface and inverted basal topography.

Where available, potential basal channels are verified using IceBridge and pre-IceBridge MCoRDS L2 ice–
180 penetrating radar (IPR) thicknesses (Paden et al., 2011, 2010) (Figs. S4–5). If a basal incision and/or surface depression does not match with a thickness minimum or a previously identified basal channel (e.g. Alley et al., 2016), we do not rule out that it could be a basal channel with entrained meltwater flow and look for other evidence of its formation.

3.3 Estimating rates of change

Time–evolving rates of change are estimated from the annual DSM mosaics in both Eulerian (fixed–coordinate system,
185 denoted by dQ/dt, where Q is the quantity in question) and Lagrangian (coordinate system moves with ice flow, denoted by DQ/Dt) reference frames. The Eulerian reference frame is used over grounded ice, to prevent slope–induced errors, and the Lagrangian reference frame is used over floating ice, where height change is dominated by horizontal advection. For Lagrangian calculations, the mosaics are flow–shifted to a common date using the smoothed annual surface velocity maps (Section 2.3) following the approach of Shean et al. (2019) and Chartrand & Howat (2020). Four epochs are defined: 2011–
190 2015, 2016–2019, 2020–2023, and the entire study period from 2011–2023. The mosaics are flow–shifted to 1 January of the earliest full year in each epoch (e.g., 1 January 2011 for the 2011–2015 epoch and the full study period).

Within each epoch, rates of change are calculated from all combinations of annual mosaics such that the relevant quantity derived from the earlier mosaic in each combination is subtracted from the later mosaic and divided by the time elapsed between the mosaics. The quantities considered are the rate of surface height change (dh/dt for grounded ice and Dh/Dt for floating ice), the rate of thickness change (dH/dt and DH_E/Dt), and the rate of basal mass loss or gain (M_b, for floating ice only). Grounded ice thickness, H, is simply the DSM–derived surface height minus the BedMachine bed height. The strip–derived annual HB from each year is used to delineate the extent of floating and grounded ice for each annual mosaic.

Flotation thickness H_E for the TGIS is derived from annual DSM mosaic freeboard heights using Eq. 1. The Lagrangian basal accumulation rate M_b (m ice equivalent a^{-1}, negative values imply melt), for floating ice is determined from mass conservation as:

$$M_b = \frac{DH_E}{Dt} = H_E(\nabla \cdot \boldsymbol{u}) - M_s) \tag{2}$$,

where M_s is the surface accumulation rate (m a^{-1}, positive for mass gain), and $\nabla \cdot u$ is the divergence in the column–average horizontal velocity of the ice $\boldsymbol{u}$ (m a^{-1}). As in Shean et al. (2019), the velocity divergence is computed at each time step as the DSM is flow–shifted, so the M_b estimate accounts for the flow history of each pixel. The rate of surface accumulation for Antarctica is obtained from the Regional Atmospheric Climate Model (RACMO) 3p2 (van Wessem et al., 2018) which provides estimates of M_s for 1979–2016 on a 27-km grid. We bilinearly interpolate the per pixel mean M_s from 2011–2016 to the mosaic grid coordinates and convert to ice–equivalent mass change rates. The maps of rates of change are smoothed by a 500 m moving mean and extreme values resulting from remaining artefacts in the annual mosaics are filtered out.

3.4 Estimating subglacial conditions

To assess potential spatial relationships between the locations where subglacial hydrologic pathways reach the GZ and align with ice–shelf basal channels, we derive a map of the subglacial hydraulic potential (ϕ) based on observations (Fig. S6) as:

$$\Phi = \rho_w gz + \rho_i gH \tag{3}$$,

where g is the acceleration due to gravity and z and H are equal to the BedMachine bed height and thickness, respectively. Assuming that water is present everywhere at the bed, we again use the TopoToolbox FLOWobj function to compute the direction that water would flow along the gradient of the hydraulic potential, and the flow accumulation ("flowacc") function to find the cumulative number of pixels that contribute to flow in each downstream pixel, and convert this to the cumulative drainage area, or basal watershed area, for each pixel along the hydraulic potential gradient. While not intended as an actual estimate of subglacial discharge, this quantity provides a relative metric of where water is likely to be routed in the subglacial system. We compare spatial patterns in inferred subglacial drainage at the GZ with the occurrence of mapped basal channels.
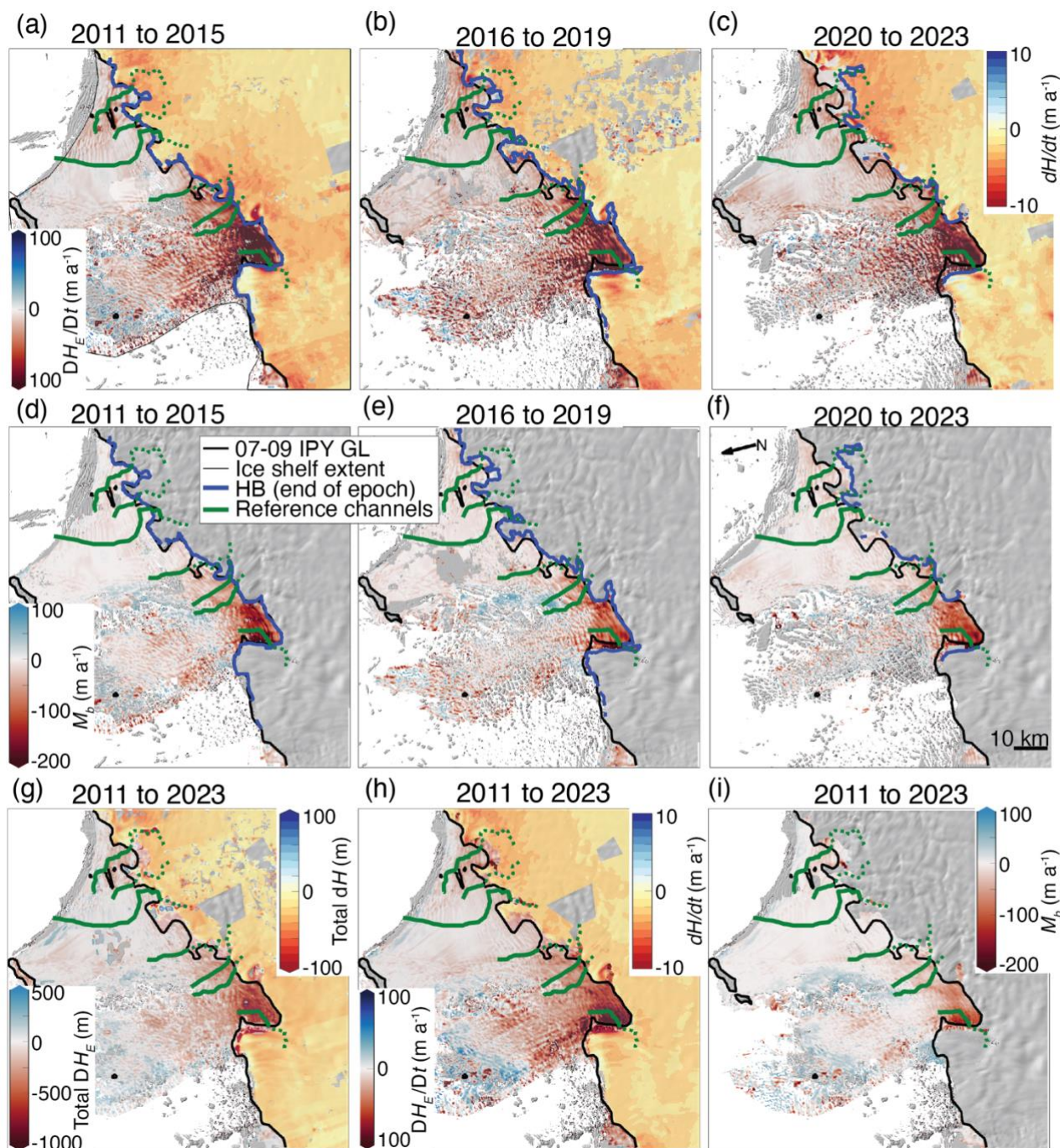
Figure 2: (a–c) Median Lagrangian rate of thickness change (DH_E/Dt) on floating ice (dark red to blue colour scale) and Eulerian rate of thickness change (dH/dt) on grounded ice (dark orange to blue colour scale) for each 4–5 year epoch. **(d–f)** Median Lagrangian basal accumulation rate (M_b, negative for melt) for each 4–5 year epoch. All maps (a-f) overlie the most recent annual mosaic hillshade from each epoch. **(g)** total Lagrangian thickness change (DH_E) on floating ice and total Eulerian thickness change (dH) on grounded ice for the entire study period. **(h)** Median DH_E/Dt and dH/dt for the entire study period. **(i)** Median M_b for the entire study

period. Maps for the entire study period (g-i) overlie the 200 m REMA mosaic. All maps show the IPY GL as a black curve, and the reference channels as green curves, and (a-f) show the most recent HB in each epoch as a blue curve.

4 Results

The TGIS has REMA coverage from November 2010 to December 2022, enabling investigation of time–evolving HB and basal channel positions as well as thinning and melt rates over the entire ice shelf at unprecedented spatial resolution (Section 4.1). The HB retreated or was stagnant everywhere in the study area (Fig. 1) and thinning and melting dominated rates of change throughout the study period (Figs. 2, S7). We identify nine regions of significant HB retreat and growth of basal cavities, labelled Cavities 1–9 (Fig. 1), discussed in more detail below (Section 4.2). Seven basal channels that originate near the GZ are consistently identified throughout the study period, labelled ThC1–7 (Fig. 1). Several of the channel locations align with inferred subglacial drainage routes (Figs. 3–5a), as discussed in more detail below (Section 4.2).
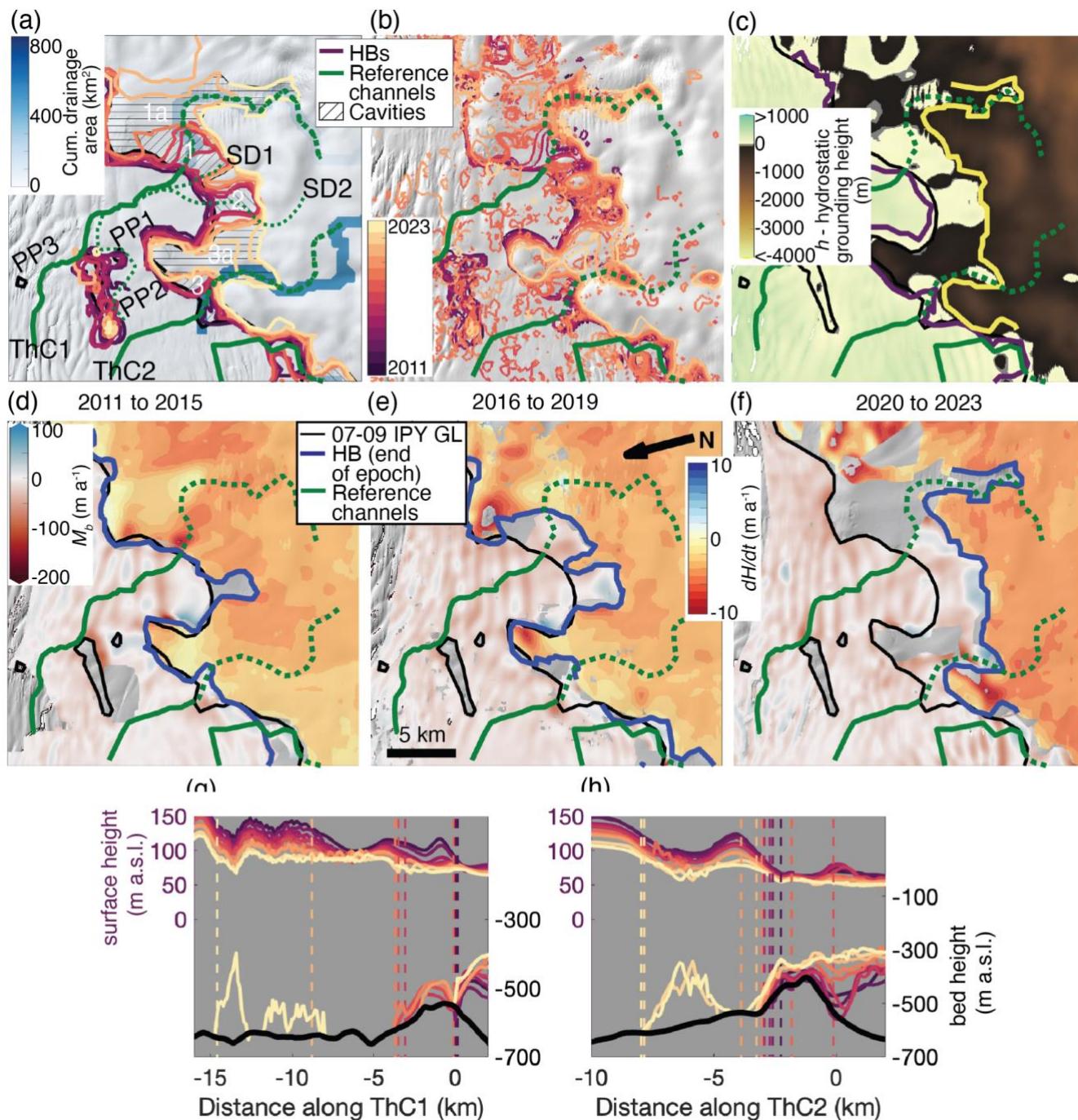
Figure 3: (a–f) Zoom on Box A from Fig. 1, showing reference channels ThC1–2 (thick green solid/dashed curves) and the 07–09 IPY GL (black curve). (a) Cumulative subglacial drainage area (blue colour scale, explained in Section 3.4) with the smoothed annual HBs (purple–orange–yellow curves, with less recent, darker features plotted below more recent features as lighter colours) and Cavities 1–3 (hatched regions). Prominent surface depressions that are possibly connected to ThC1 are highlighted by thin dotted

240

green curves. (b) Unfiltered HB features for each year (also on the purple–orange–yellow colour scale used for smoothed annual HBs). Panels (a) and (b) use the REMA v4 200 m mosaic hillshade as the base map. (c) Difference between the 2019 surface height and the hydrostatic grounding height (which is the flotation thickness plus the BedMachine v3 bed height) overlain by the smoothed annual HBs from 2011 (purple curve) and 2023 (yellow curve). (d–f) M_b on the TGIS (dark red to blue colour scale) and dH/dt on grounded ice (dark orange to blue colour scale) for each 4–5 year epoch overlain on the most recent annual REMA mosaic hillshade from each epoch. The most recent HB in each epoch is also plotted (blue curve). Annual surface height (left axis) and ice base (right axis) and BedMachine bed height (right axis, black curve) interpolated to reference channels (g) ThC1 and (h) ThC2. Vertical dashed lines mark the most landward intersection of each year's HB with the extended channel. Distances are defined from each channel's intersection with the IPY GL, with positive distance indicating advance and negative distance indicating retreat.

4.1 Time–evolving rates of basal mass change and ice thickness

Figures 2–5 indicate that rates of basal mass change are dominated by melting but are spatially and temporally variable throughout the observation period, as are rates of thickness and surface–height change (Table 1). In general, thinning and melting accelerated from 2011–2015 to 2016–2019 and decelerated slightly in 2020–2023. The banded patterns of positive and negative values visible on the TEIS and TWIT in maps of DH_E/Dt and M_b may be due to changes in ice velocity not accounted for in flow–shifting using annual surface–velocity maps, or due to hydrostatic compensation around growing basal crevasses (e.g. Vaughan et al., 2012).

Overall, the TEIS experienced less basal melting than the TWIT. Nevertheless, there was some apparent mass gain in areas of TWIT, particularly in the downstream portion of the TWIT and the shear zone between the TEIS and TWIT (Figs. 2, 4–5). We expect that the apparent positive M_b in the downstream portion of the TWIT may be due to transient grounding, as evidenced by the presence of isolated HB features in that region (Figs. 5b, S4b). The fastest rates of thinning and melting on the TEIS consistently occur at the eastern ends of pinning points PP2 and PP4, with PP2 located near a zone of rapid HB retreat (Section 4.5) and the opening of Cavity 3 (Fig. 2, Sections 4.2.1 and 4.2.4, respectively).

The main trunk of the TWIT near the GZ experienced the most intense melting at rates exceeding 250 m a^{-1} in places throughout the study period (Fig. 5). A closer look within Box B (Fig. 4d–f) shows that consistently high melt rates also occurred near the GZ in the vicinity of ThC5 and Cavity 7. There is also a flow–parallel band of accelerating thinning and melting along ThC6 near a zone of modest HB retreat along the most pronounced inferred subglacial drainage route (Figs. 2, 5d–f, Section 4.2.3).

Table 1. Rates of change in each annual mosaic epoch. All values are in units m a^{-1} (ice equivalent).

	Rate of surface height change		Rate of thickness change				Rate of basal mass change	
	Floating Dh/Dt		Grounded dH/dt		Floating DH_E/Dt		Floating M_b	
	Mean $\pm \sigma$	median	Mean $\pm \sigma$	median	Mean $\pm \sigma$	median	Mean $\pm \sigma$	median
Overall	-0.7 ± 4.9	-0.9	-2.2 ± 0.7	-2.1	-14.2 ± 27.7	-8.6	-6.2 ± 27.9	-3.1
2011-2015	-1.0 ± 6.3	-0.8	-2.8 ± 1.6	-2.6	-21.4 ± 36.9	-11.0	-14.5 ± 37.4	-6.2
2016-2019	-3.0 ± 5.0	-2.0	-2.4 ± 2.2	-2.3	-27.3 ± 35.6	-17.8	-19.0 ± 37.6	-11.1
2020-2023	-2.7 ± 5.1	-1.8	-2.0 ± 2.0	-1.9	-26.2 ± 35.3	-16.2	-16.8 ± 34.8	-9.2

4.2 Basal channel–HB interactions

As mentioned above, the HB retreated or stagnated relative to the IPY GL everywhere, including on pinning points, with significant variability in the rates of retreat. While few consistent spatiotemporal patterns in HB retreat emerged, there were no areas of sustained HB advance.

We identify several persistent basal incisions and surface depressions along seven basal channels. We reduce the impact of noise in individual DSM strips on mapped basal incisions and surface depressions (Fig. S4) by defining fixed reference locations of seven basal channels, called ThC1–7, shown as green curves in figures, to be where the greatest overlap of these features occurs. The reference channels are extended above the GZ along surface depressions (where present) on grounded ice, shown as thick dotted green curves in figures, enabling us to measure changes in surface height (Figs. 2–5g–i), thickness (Fig. 6b) and velocity (Figs. 6 and 7) along the reference channels, as well as changes in their intersections with the HB from each year relative to their intersections with the 07–09 IPY GL (Figs. 3–6), referred to as the ThCX–IPY GL intersection. IceBridge MCoRDS ice–thickness profiles were queried to verify the presence of the eight basal channels identified, although data quality along some profiles is poor (Figs. S4–5). There are also several persistent surface depressions that extend upstream of the IPY GL but do not appear aligned with mapped basal channels, labelled SD1–7 and marked by thin dotted green curves in Figures 3a and 5a.

A variety of behaviours and interactions between the basal channels and the GZ are observed. We distil these into three major types:

1. Narrow–cavity HB retreat along a narrow band parallel to a basal channel (ThC2, ThC3, ThC5; Section 4.2.1)
2. Wide–cavity retreat along a basal channel (ThC1, ThC4; Section 4.2.2)
3. Little to no HB retreat at the upstream ends of basal channels (ThC6, ThC7; Section 4.2.3).

295   Figure 6a shows a time series of the change in position of the HB's intersection along each reference channel and illustrates that Type 1 retreat tended to involve more steady retreat and Type 2 retreat tended to involve rapid retreat followed by stabilisation. It is important to note that we do not consider these types to be mutually exclusive, as more than one type of HB retreat is observed along several basal channels throughout the study period.

        Several TGIS–wide similarities among basal channels are observed. The grounded ice within ~5 km of each channel's
300   upstream end had background thinning rates between -1 to -4 m a^{-1} (Figs. 2a–c, 3–5d–f). All channels except for ThC4 originate near areas of high cumulative subglacial drainage area at the GZ (Figs. 3–5a). Retreat of the HB exceeding 1 km occurred along all reference channels except for ThC6 and thinning and melting occurred near all channel intersections with the GZ by the end of the study period (Figs. 2–6). Notably, the mean velocity along each HB is slightly slower at the ThCX–HB intersections than in non–channelized portions of the GZ (Fig. 6c). However, no strong relationships emerge between velocity
305   and HB retreat rates along each channel (Fig. 7).
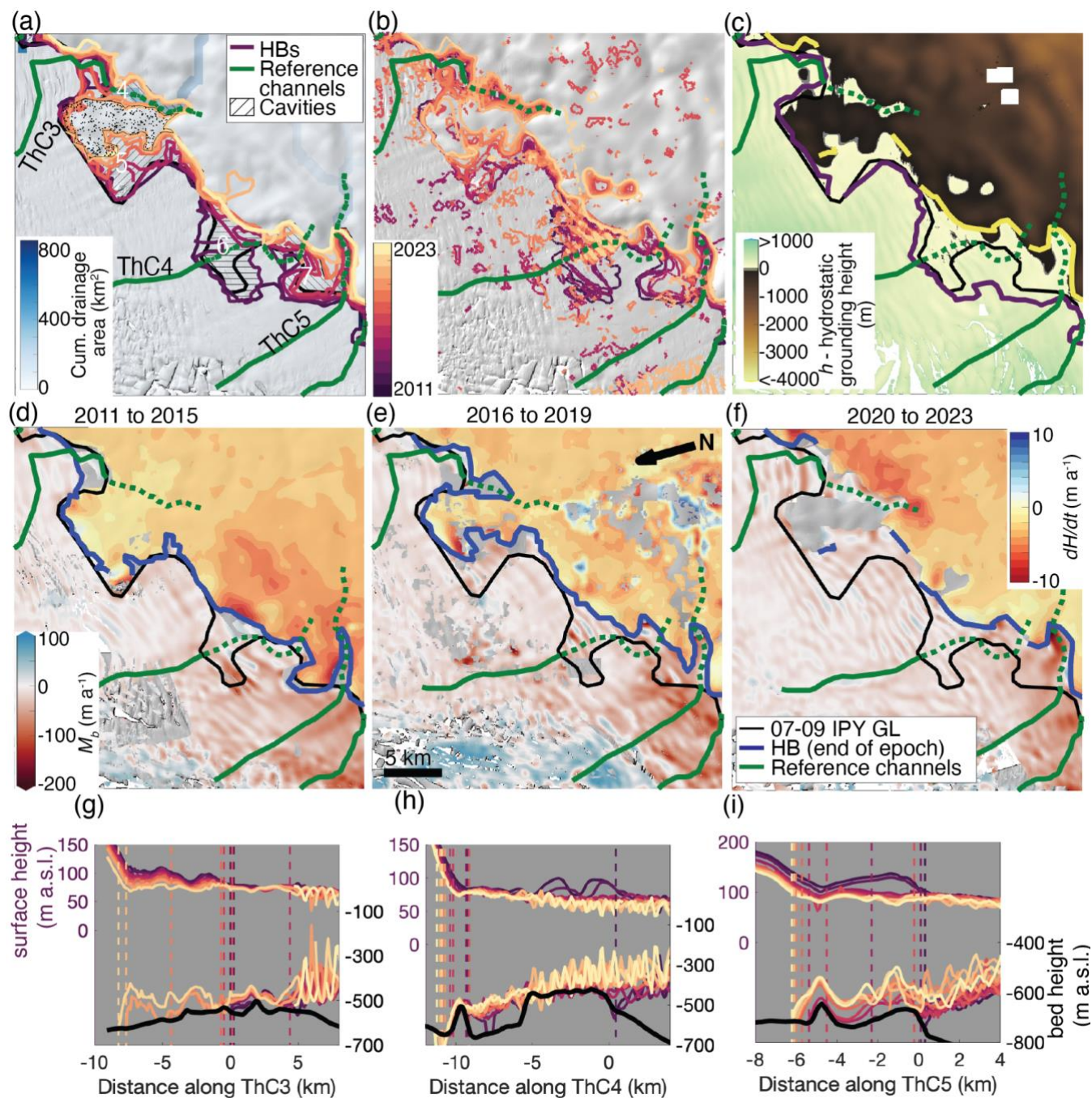
Figure 4: (a–f) Zoom on Box B from Fig. 1, showing reference channels ThC3–5 (thick green solid/dashed curves) and the 07–09 IPY GL (black curve). **(a)** Cumulative subglacial drainage area (blue colour scale) with the smoothed annual HBs (purple–orange–yellow curves, with less recent, darker features plotted below more recent features as lighter colours) and Cavities 4–7 (hatched regions). **(b)** Unfiltered HB features for each year (also on the purple–orange–yellow colour scale used for smoothed annual HBs). Panels (a) and (b) overlie the REMA 200 m mosaic hillshade. **(c)** Difference between the 2019 surface height and the hydrostatic grounding

height overlain by the smoothed annual HBs from 2011 (purple curve) and 2023 (yellow curve). (d–f) Mb on the TGIS (dark red to blue colour scale) and dH/dt on grounded ice (dark orange to blue colour scale) for each 4–5 year epoch overlain on the most recent annual REMA mosaic hillshade from each epoch. The most recent HB in each epoch is also plotted (blue curve). Annual surface height (left axis) and ice base (right axis) and BedMachine bed height (right axis, black curve) interpolated to reference channels (g) ThC3, (h) ThC4, and (i) ThC5. Vertical dashed lines mark the most landward intersection of each year's HB with the extended channel. Distances are defined from each channel's intersection with the IPY GL, with positive distance indicating advance and negative distance indicating retreat.

4.2.1 Type 1: Sustained retreat along narrow cavities

Channels ThC2, ThC3, and ThC5, as well as ThC1 in more recent years, were associated with steady, sustained HB retreat along narrow cavities. These features are each directly aligned with an inferred subglacial drainage pathway (Figs. 3–5a) along which HB retreat occurred, such that the cavities may strike oblique to the flow direction, but parallel to the surface depressions. Furthermore, the profiles for these reference channels show large undulations in bed and surface height within 5–10 km of their intersections with the IPY GL grounding line (Figs. 3–4g–i) which make it difficult to interpret DH/Dt and M_b in these cavities because the flow–shifting does not fully account for height changes due to horizontal advection, leading to alternating bands of apparent thinning/melting and thickening/mass gain near the GZ (Figs. 3–4d–f).

The HB intersection with ThC2 predominantly exhibited Type 2 retreat as the HB retreated in a narrow band along the sinuous ThC2 and its inferred underlying subglacial drainage route throughout the study period (Fig. 3). Cavity 3 widened suddenly following a few years of retreat in a narrow band, temporarily exhibiting Type 2 characteristics, before growing further upstream in a narrow band. Between 2021–2023, continued HB retreat opened all of Cavity 3a so that it merged with Cavity 2 (Fig. 3a), coinciding with a 20% increase in surface velocity along ThC2 after relatively steady speeds in earlier years (Fig. 7). Figures 5c and 5h show that Cavity 3a overlies a bedrock ridge, and that the upstream end of ThC2 overlies a deepening trough. Rapid thinning and basal melt occurred near the intersection between ThC2 and the GZ throughout the study period (Figs 3d–f).

The HB position change along ThC3 exhibits the clearest example of Type 1 retreat (Figs. 1, 4). Figures 4a–b and 4g show that the HB remained relatively stationary relative to ThC3 on a small bedrock ridge through 2018, before retreating rapidly along ThC3 down a retrograde bed slope at a rate of 3.5 km a^{-1} between 2018–2020, opening the narrow Cavity 4 (Fig. 3a). HB retreat slowed in subsequent years despite the retrograde bed slope continuing upstream. Despite the banded pattern in the melt rate maps in this region, it appears that melt rates generally intensify throughout the study period (Figs. 4d–f). As observed along ThC2, surface velocity along ThC3 accelerated between 2020–2023, although retreat had slowed by this time (Fig. 7).

Figure 4 shows that the HB retreated south–eastward along ThC5 at an average rate of ~0.7 km a^{-1} between 2013–2018, forming the finger–like southern portion of Cavity 7. During this time, thinning and basal melt rates reached 100 m a^{-1} and 60 m a^{-1}, respectively, (Figs. 4d–e) along ThC5 as the HB breached successive bedrock ridges before stagnating on a relatively flat bed about 5–7 km up–glacier of the ThC5–IPY GL intersection (Fig. 4i). Although the HB didn't retreat much

further along ThC5, Cavity 7 widened eastward and merged with Cavity 6. During this time, basal melt rates within Cavity 7 intensified, exceeding 100 m a^{-1} along the ThC5 (Fig. 4f).

350
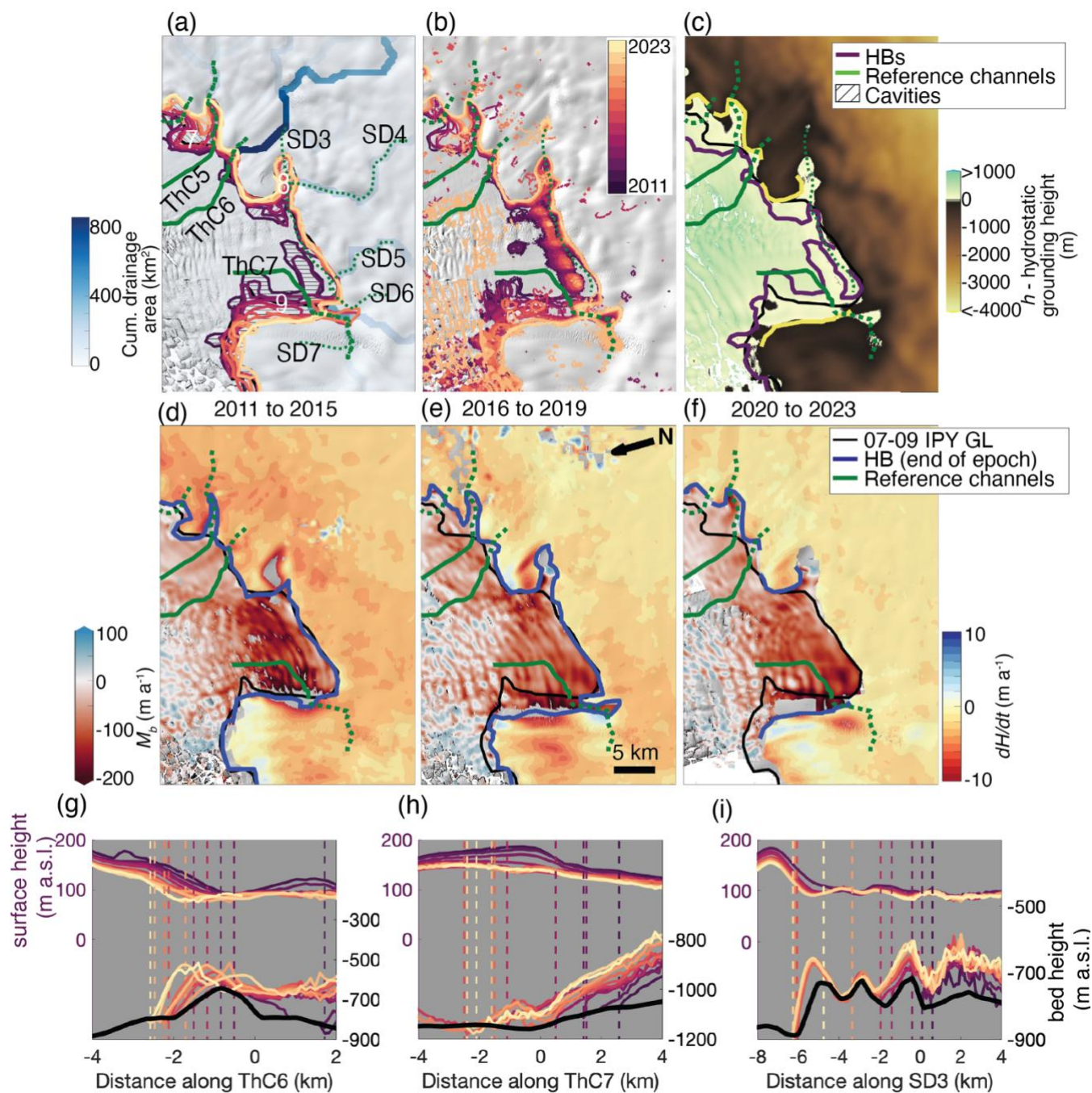
Figure 5: (a–f) Zoom on Box C from Fig. 1, showing reference channels ThC6–7 (thick green solid/dashed curves) and the 07–09 IPY GL (black curve). (a) Cumulative subglacial drainage area (blue colour scale) with the smoothed annual HBs (purple–orange–yellow curves, with less recent, darker features plotted below more recent features as lighter colours) and Cavities 7–9 (hatched regions). Prominent surface depressions SD3–7, some of which are possibly connected to ThC7, are highlighted by thin dotted green curves. (b) Unfiltered HB features for each year (also on the purple–orange–yellow colour scale used for smoothed annual HBs). Panels (a) and (b) overlie the REMA 200 m mosaic hillshade. (c) Difference between the 2019 surface height and the hydrostatic

grounding height overlain by the smoothed annual HBs from 2011 (purple curve) and 2023 (yellow curve). (d–f) M_b on the TGIS
(dark red to blue colour scale) and dH/dt on grounded ice (dark orange to blue colour scale) for each 4–5 year epoch overlain on the
360   **most recent annual REMA mosaic hillshade from each epoch. The most recent HB in each epoch is also plotted (blue curve). Annual**
surface height (left axis) and ice base (right axis) and BedMachine bed height (right axis, black curve) interpolated to reference
channels (g) ThC6, (h) ThC6, and (i) SD3. Vertical dashed lines mark the most landward intersection of each year's HB with the
extended channel. Distances are defined from each channel's intersection with the IPY GL, with positive distance indicating advance
and negative distance indicating retreat.

365

4.2.2 Type 2: Wide–cavity retreat

Channels ThC1 and ThC4 are associated with sudden, rapid HB retreat off of bedrock highs to form wide Cavities 1a, 2, and
6, respectively (Figs. 3–4). Expansion of these relatively large cavities mostly occurred during 2013–2016 as widening across–
flow.

370   ThC1 and merging surface depressions SD1 and SD2 intersect the IPY GL in a region where the TEIS cavity is deeply
embayed. Figure 3a shows that Cavity 1 opened up as the HB retreated suddenly along the ThC1 surface depression and an
inferred subglacial channel between 2015 and 2016, and that Cavity 2 opened up as the HB retreated suddenly along SD2
(which does not align with an inferred subglacial channel) between 2014 and 2015, forming the lobes that make this region
known as the "butterfly" region. At the same time, the velocity along ThC1 accelerated after a period of stability between
375   2011–2015 and continued to accelerate throughout the study period (Fig. 7). As basal melt rates accelerated to near 40 m a^{-1}
by 2016–2019 (Fig. 3e), Cavities 1 and 2 widened but did not extend further upstream (Fig. 3a). Cavity 2 merged with Cavity
1 between 2021–2022, eliminating the butterfly shape that was prominent in earlier years. After 2019, the HB exhibited Type
1 retreat, as the narrower Cavity 1a extended upstream along the ThC1 surface depression and underlying inferred subglacial
channel at a rate exceeding 2 km a^{-1} (Figs 3, 6a).

380   ThC4 is situated near the western edge of the TEIS and does not align with an inferred subglacial hydrological route.
ThC4 appears to result from the merging of two incisions initiated at two bedrock ridges, the wider of which is located at -5
to 0 km along ThC4 in Figures 4h and 7 (where 0 km is the northernmost ThC4–IPY GL intersection); the narrower ridge is
located further south at about -9.2 km in Figures 4h and 7, near the western end of Cavity 7 (Fig. 4a). Several instances of the
sinuous surface depression persist across Cavities 6 and 7 (Fig. S4c), while instances of the basal incision appear to curve
385   around Cavity 6 (Fig. S4a). Figure 4h shows that Cavity 6 opened along ThC4 between 2011–2015 as ice ungrounded from
the wide ridge. In subsequent years, Cavity 7 reached its eastern and southern maximum extents and merged with Cavity 6 as
the HB retreated off the narrower southern bedrock ridge (Figs. 4a, 4h). Despite basal melt rates consistently exceeding 60 m
a^{-1} near ThC4 (Fig 4d–f, which may be unreliable due to possible intermittent re–grounding, indicated by the isolated HBs in
Figure 4b), the HB did not retreat much further along ThC4, stabilising within a bedrock trough (Fig. 4h). The velocity along
390   ThC4 was highly variable, decelerating by about 5% as Cavity 6 grew, accelerating by about 10% between 2015–2016, slowing
again between 2016–2019 as Cavity 7 grew, and speeding up, especially downstream of Cavity 6, as the HB stagnated (Fig.
7).
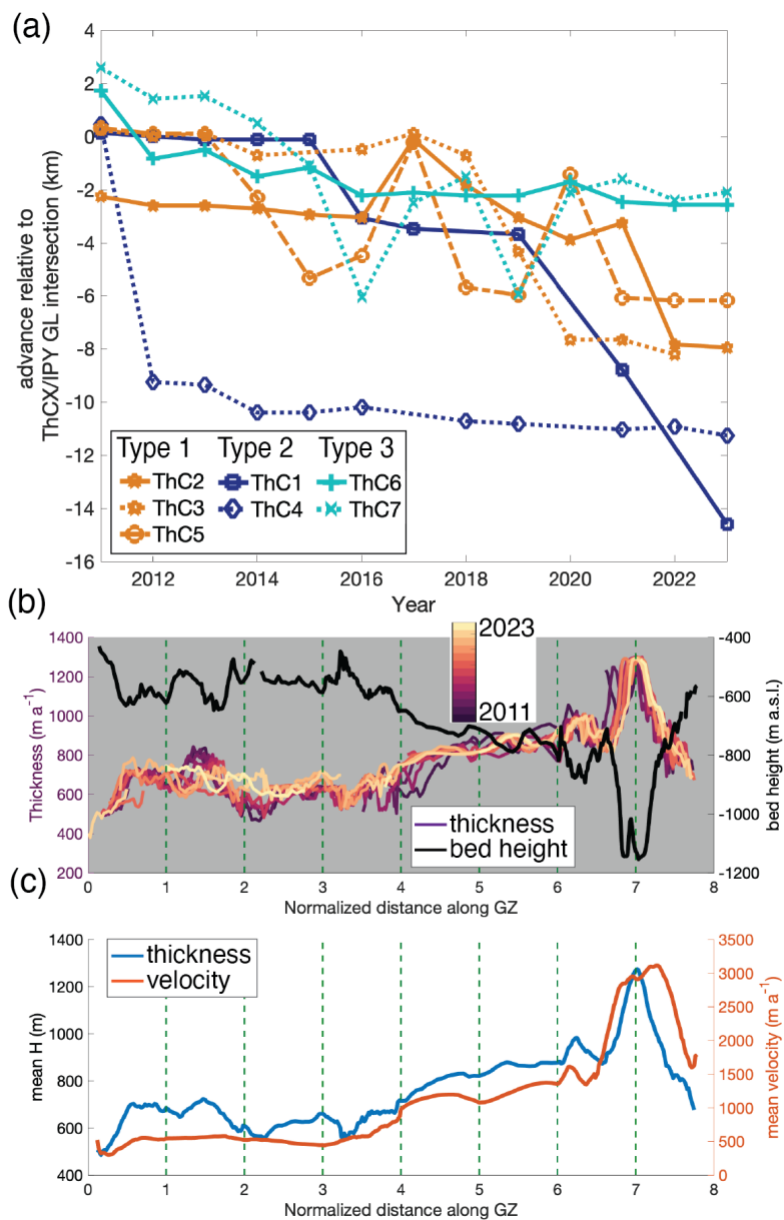
Figure 6: (a) Time series of HB position along each reference channel, with negative distance indicating retreat, and 0 km marking the ThCX/IPY GL intersection. The orange time series indicate Type 1 retreat, the blue time series indicate Type 2 retreat, and the teal time series indicate Type 3 retreat. (b) Annual thickness and (c) mean thickness and velocity along the HB, with unitless distance normalised to the intersection of each year's HB with each basal channel ThC1–7.

4.2.3 Type 3: Little to no HB retreat

Basal channels ThC6 and ThC7 were associated with modest HB retreat that did not fit into Type 1 or Type 2 cavity shapes, despite their alignment with inferred subglacial drainage routes (Fig. 5).

ThC6 is aligned with the strongest inferred subglacial channel just east of the TWIT GZ embayment, but the surface depression does not appear to extend upstream of the IPY GL (Figs. 4a, S4c). Thus, the upstream end of the ThC6 reference channel was extended past the GZ arbitrarily. Throughout the study period, rapid thinning and basal melt occurred near the ThC6–IPY GL intersection (Fig. 5d–f). The HB retreated at a rate of about 0.3 km a^{-1} along ThC6 (Fig. 6a), and the small cavity forms a v–shape along the inferred subglacial channel (Fig. 5a), potentially indicating that Type 2 retreat will occur in the future. ThC6 also experienced among the widest fluctuations in velocity, although there was no clear relationship between velocity and HB retreat or rates of thinning (Fig. 7).

The western GZ of the TWIT embayment exhibits complex morphology and changes, but relatively slow rates of retreat in the vicinity of ThC7 and merging surface depressions SD6–7 (Fig. 5a). At ThC7, the HB retreated ~0.4 km a^{-1} as Cavity 9 extended westward between 2013–2023, consistently thinning and melting at rates exceeding 100 m a^{-1} (Figs. 5, 6a). Notably, in 2016 and 2019, the HB temporarily retreated along a narrow band along the ThC7 surface depression (Fig. 5i), within the same timeframe as a 300 m a^{-1}, or 11%, increase in velocity between 2016–2020 (Fig. 7).
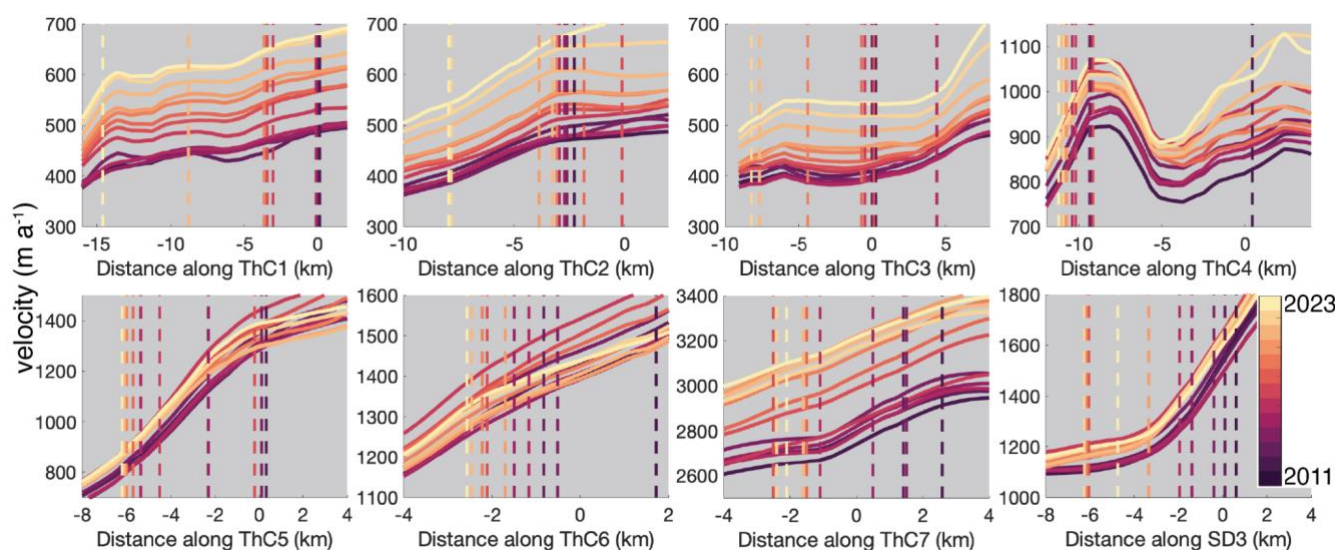
Figure 7: MEaSUREs annual velocity (2011–2015) and averaged summer quarterly velocities from InSAR (2016–2023) interpolated to reference channels ThC1–7 and SD3. Vertical dashed lines mark the most landward intersection of each year's HB with the reference channel. Distances are defined from each channel's intersection with the IPY GL, with positive distance indicating advance and negative distance indicating retreat.

4.2.3 Retreat not associated with basal channels

There are a few regions where HB retreat is observed in the absence of basal channels and/or inferred subglacial drainage routes. Between ThC3 and ThC4, there is a region where the HB shifts eastward between 2013 and 2021 at a rate of up to 0.6
425   km a^{-1}, opening Cavity 5 (Fig. 4). Notably, the 2022 HB connects with Cavity 4, indicating that a larger cavity may have opened, but there was insufficient coverage to map the 2023 HB in this region (stippled area in Fig. 4a). Since the 2022 HB could have resulted from the coverage of an individual strip, or an error in the manual delineation of the annual HB, we do not consider that entire region to be ungrounded in 2022.

The main trunk of the TWIT exhibited complex HB changes seemingly independent of ThC7. Merging surface
430   depressions SD3 and SD4 are identified upstream of the south–eastern corner of the embayed GZ in the main trunk of the TWIT and appear to be associated with HB retreat (Fig. 5a, S4c). SD4 aligns with an inferred subglacial channel, but SD3 does not (Fig. 5a). We also identify a surface depression extending from SD3 and SD4 parallel to the IPY GL at the southern boundary of the TWIT, but IPR transects M6 and M7 do not indicate that there are corresponding basal incisions (Fig. S5). The surface depression extending across the TWIT may instead be a dynamical response to the transition of flow off the ridge
435   along the southern boundary of the GZ embayment (Fig. S8a). Figures 5 and 6a show that the HB retreated along SD3 at an average rate of ~0.8 km a^{-1} between 2011–2018, opening the narrow Cavity 8 along an undulating bedrock topography. The fastest retreat rates (~2 km a^{-1}) occurred between 2015–2017, followed by relative stability over a bathymetric low after 2018. Melt rates and thinning rates were consistently high at the downstream end of Cavity 8, exceeding 100 m a^{-1} along the IPY GL in all three multiyear epochs (Figs. 5d–f).

440   Figure 5b shows that the TWIT contained many small, isolated HBs throughout most of the study period that may indicate intermittent grounding, although the bed height is unreliable here due to the use of indirect measurements for bed heights in ice–shelf cavities (Fig. S8, (Morlighem et al., 2020). The annual HBs from the early years of the study period extended eastward in a narrow band between ThC7 and the IPY GL, narrowing the ice–shelf cavity in the centre of the TWIT to only 2.5 km (Figs. 5a–b). By 2013, Cavity 9 had opened and the HB was approximately at the same location as the IPY GL
445   along the southern margin of the TWIT embayment. Furthermore, the western edge of the TWIT GZ embayment retreated steadily to the west and up a slope in the basal topography throughout the study period (Figs. 5a, S8a). The western edge of the embayment also experienced high rates of thinning and basal melting throughout the study period as Cavity 9 opened (Fig. 5d–f).

4.3 Pinning points

450   The HBs at the pinning points exhibited a variety of behaviours. Our HBs maps did not capture PP3, although PP1, PP2, and PP4–6 were mapped. We only map PP1 through 2014, and PP2 grew smaller through 2023 (Fig. 3). Pinning points 1 and 2 experienced relatively high rates of thinning and basal melting at the eastern extent of the IPY GL of PP2 (Figs. 2, 3d–f). Furthermore, ThC1 possibly rerouted as these pinning points shrank; from 2011–2014, the surface and basal manifestations of

ThC1 curved toward the west, following the western prong of the "y" shape south of PP1, then straightened toward the eastern
455   prong of the "y" shape between 2015–2022 (Fig S4).

Pinning points 4 and 5 were mapped throughout the study period, without much change in HB position, and
experienced thinning and melting at rates similar to the rest of the TEIS (Figs. 1–2). We observe possible north–westward
growth of PP4 and PP5 but note that BedMachine is poorly constrained here (Fig. S8). Pinning point 6 was also mapped
throughout the study period, although it is largely indistinguishable from other small, noisy HBs that are mapped, but filtered
460   out, on the bedrock high in that region (Figs. 1, S4d).

As discussed in Section 4.2.3, the unfiltered HBs in the TWIT (Fig. 5b) indicate the presence of many small pinning
points, which appear to shrink or disappear over time as the ice thins. However, as noted elsewhere, the bed topography is
poorly constrained in this cavity so the locations of HBs and basal incisions inferred using the hydrostatic assumption are
uncertain. Notably, the TWIT lost an area of ~1270 km² between 2011–2012, retreating from potential pinning points near the
465   front, and continued to lose area throughout the study period (Fig. S2).

5 Discussion

This work reveals high–resolution observations of important processes affecting the shape and structure of the Thwaites
Glacier and TGIS. We observe evidence for high rates of GZ retreat along ice–shelf basal channels and upstream subglacial
channels on the Thwaites Glacier and TGIS using REMA DSMs to map basal channels, surface depressions, and rates of
470   thickness and basal mass change. We observe three major types of retreat along seven basal channels and associated surface
depressions: narrow–cavity retreat, wide–cavity retreat, and little to no retreat. Regions associated with each type of retreat are
often collocated with high rates of ice–shelf basal mass loss and thinning both up– and down–stream of the GZ, particularly
in the 2011–2015 epoch.

5.1 Melt Rates

475   Aside from some differences in magnitude, the general patterns of persistent retreat and rapid thinning and basal melt along
the Thwaites Glacier GZ that we observe are in agreement with other recent observations (e.g. Holland et al., 2023; Milillo et
al., 2019; Schmidt et al., 2023; Adusumilli et al., 2020). All confirm that M_b is consistently smaller in magnitude on the TEIS
than the TWIT, and that more melting occurs near the GZ than further seaward. Others have also observed and modelled rapid
and potentially unstable retreat of the GZ, attributed to enhanced sub–ice shelf melting (Joughin et al., 2014; Rignot et al.,
480   2014; Seroussi et al., 2017; Yu et al., 2018; Milillo et al., 2019; Hoffman et al., 2019). Enhanced basal melt rates are in turn
attributed to the intrusion of warm Circumpolar Deep Water (CDW) flowing along bathymetric troughs to the GZ (Nakayama
et al., 2018; Milillo et al., 2019; Hogan et al., 2020). In the TGIS region, CDW intrusion primarily occurs along two bathymetric
troughs (indicated in Fig. 1), allowing it to reach the GZ of both the TEIS and the TWIT (Dutrieux et al., 2014; Dotto et al.,
2022).

485   The modest basal melt rates that we observe in the vicinity of Cavities 1, 1a, and 2 (Fig. 3d–f) are largely in agreement with those observed by the Icefin submersible in the same region (Schmidt et al., 2023). Holland et al. (2023) show modest apparent basal mass gain along the eastern and southern GZs of the TWIT embayment in 2011 and melt rates reaching 250 m a^{-1} along the southwestern boundary in both 2011 and 2022. High rates of apparent basal mass gain in the TWIT are also inferred by Milillo et al. (2019). We observe basal melt rates reaching 250 m a^{-1} throughout the TWIT, especially at the

490   southwestern GZ, but we observe no basal mass gain at the southern GZ. We suggest that the choice of Lagrangian flow–shifting methods can result in apparent mass gain in the TWIT if the time–evolving flow divergence is not accounted for (Fig. S9). Milillo et al. (2019) posit that, as the ice thins and the grounding line retreats, the bending zone where the ice is deflected below flotation before rebounding also retreats, causing changes at the surface to mask the true magnitude of ice thinning and overestimate M_b. With the caveat that BedMachine is poorly constrained in this ice–shelf cavity (Fig. S8) we also see

495   intermittent re–grounding of ice in the raw HB features (Figs. 5b, S4d), which would further complicate the actual hydrostatic rebound, as well as the hydrostatic assumption and assumptions about ice flow. These factors all reduce confidence in the inferred DH/Dt and M_b in the TWIT embayment.

5.2 Hydrostatic Boundaries

In agreement with other studies, we find a mix of stagnation and retreat of the HB along the entire coast of the TGIS.

500   The fastest retreat rates are collocated with retrograde slopes in the bed topography, basal channels that intersect the IPY GL and/or the positions of inferred subglacial channels, and high basal melt rates. Notably, our rates of thinning and HB retreat for the fast–flowing TWIT align closely with those of Milillo et al. (2019), who showed that the grounding line along the western margin of the TWIT embayment (what we call Cavity 9; near points A and B in Fig. 1 in Milillo et al. (Milillo et al., 2019)) retreated at a rate of 0.6 km a^{-1} to the west between 2011 and 2017. Our results also align with those of Bevan et al.

505   (2021), who documented the opening of an ice–shelf cavity along the retreating western margin between 2014 and 2017. We also find HB retreat rates of 0.3–0.6 km a^{-1} between 2011–2019 and basal melt rates reaching 180 m a^{-1} as Cavity 9 opened. Milillo et al. (2019) attributed the rapid ungrounding at their point A to its prograde slope, which favours CDW intrusion and efficient cavity opening, consistent with plume theory (Jenkins, 2011).

ThC2, ThC3, ThC5, and SD3 are associated with Type 1 HB retreat in narrow bands oblique to the flow direction,

510   but parallel to inferred subglacial channels, lending confidence to our predicted subglacial channel distribution and indicating that subglacial melting is strong (Figs. 3–5). Similar retreat along subglacial channels has been observed on Nioghalvfjerdsfjorden Glacier (N79) Ice Tongue in northeast Greenland (Narkevic et al., 2023) and the Petermann Glacier Ice Tongue in northwest Greenland (Ciracì et al., 2023), although in both cases, retreat occurred in narrow bands aligned with the direction of ice flow. Hager et al. (2022) showed that the inclusion of channelized drainage into their model increased effective

515   pressures in non–channelized regions near the grounding line, which may increase basal drag and reduce grounding line retreat and mass loss (Yu et al., 2018) and velocities on Pine Island Glacier (Gillet-Chaulet et al., 2016; Joughin et al., 2019). We observe little to no retreat where subglacial channelization is not present, which may be due to high points or prograde slopes

in the bed topography but could possibly be due in part to enhanced basal friction in the absence of subglacial water or its concentration within subglacial channels. It is expected that melt rates are higher where discharge of subglacial meltwater occurs (e.g. Le Brocq et al., 2013; Washam et al., 2019). The volume from basal melt has been estimated at 3.5 Gt for the 189,000 km² Thwaites Glacier drainage basin (Joughin et al., 2009), so ample subglacial water is available, and may discharge in the manner we predict (Figs. 3–5a, S4b), forming a collection of basal channels when it reaches the ice shelf (Section 5.3). While we do not investigate evolution of the subglacial cumulative drainage area over time, we posit that any discrepancies in orientation or position among mapped surface depressions and basal incisions may be due to rerouting of the subglacial drainage system.

In contrast with the retreat observed along the continuous continental GZ and shrinking or ungrounding of pinning points 1, 2, and 3, PP4 and PP5 exhibit signs of growth throughout the study period, particularly with advance to the northwest of their IPY positions (Figs. 1, S4) Indeed, the bed topographic high on which these pinning points rest extends and grows taller to the northwest (Fig. S8a), and some localised thickening is observed as the TEIS flows onto PP5, although the region is dominated by thinning and melting (Fig. 2). Due to gaps in coverage (Fig. S2), it is difficult to tell whether the ice–shelf area to the north of the pinning points is changing. Wild et al. (2022) demonstrate that although PP5 is structurally sounder than PP4, the two used to be connected and their separation and the disconnection of the TEIS and TWIT has altered ice flow. This change, along with the advection of thinner and more damaged ice on the TEIS portends ungrounding from the pinning point within the next decade (Wild et al., 2022).

The unfiltered and unsmoothed HBs observed throughout the Thwaites Glacier and TGIS provide insight into potential future behaviour. We observe isolated HBs upstream of the continental GZ, indicating that the ice surface is below the "hydrostatic grounding height" (ice surface height resulting from adding the flotation thickness H_E for all ice to the bed height, Figs. 3–5b–c) above bedrock lows. The bed heights from BedMachine v3 are relatively reliable upstream of the IPY GL, with errors < 50 m (Fig. S8b), which is similar to the uncertainty in our calculation of H_E, promoting confidence in the existence of pockets where the surface is below grounding height upstream of the GZ. Several of the isolated HBs upstream of the GZ persist over multiple epochs and align with inferred subglacial drainage pathways. The isolated HBs upstream of the IPY GL are necessarily located at bed topographic lows, and likely contribute to the cycle of rapid retreat and temporary stabilisation observed along several reference channels. Indeed, Figures 3–5b show that the continental HB retreated far enough for several cavities to encompass some of these isolated HBs from earlier epochs. Notably, the GZ near ThC6, which aligns with the inferred subglacial channel location with the highest flow accumulation, experienced modest HB retreat but high rates of thinning and ice–shelf melting (Fig. 5), potentially foreshadowing the formation of a Type 2 cavity; however, there are few isolated HBs further upstream (Fig. 5b–c). Furthermore, high rates of thinning in the vicinity of a few of these upstream HBs (in and around Cavities 1a, 6, 8, and 9) may indicate ocean–induced melting above the GZ, as observed on Petermann Glacier (Gadi et al., 2023). We do not observe any increased melt rates or thinning for most of these closed regions, however, even when they are near the main HB, suggesting there is little incursion of seawater that might enhance melt for most of the glacier.

We also observe isolated HBs throughout the TWIT, indicating that the ice surface is above the hydrostatic grounding height above bedrock highs (Figs. 3–5b–c). In contrast to our certainty in mapping isolated HBs above the GZ, BedMachine errors increase rapidly to 400 m downstream of the IPY GL, where the bed is inferred from gravity inversion, so we are less confident in the existence of additional pinning points within the TGIS. We expect that the isolated HBs that persist on high

555   points within ~2 km downstream of the IPY GL throughout several years (where BedMachine errors are around 100 m, Fig. S8b), may have been or currently are pinning points. Likewise, we expect sufficiently high points between the isolated HBs upstream of the GZ (Figs. 3–5b, S8) to serve as temporary pinning points as new cavities open around them as the continental HB retreats.

5.3 Basal Channels

560   Based on our inferred subglacial drainage pattern and mapped surface depressions and basal incisions, we suggest that all basal channels identified in this study except ThC4 are subglacially sourced. Ice–shelf basal channels have been mapped previously on the TGIS by Alley et al. (2016), and several subglacial channels were also identified by Milillo et al. (2019), many of which align with our DSM–derived channel positions. Comparisons between these observations provide insights into the formation of each basal channel.

565   There is relatively strong evidence that ThC1 is a subglacially–sourced basal channel. The downstream end of ThC1 is about 6 km away from a basal channel identified by Alley et al. (2016) (Fig. S10), and its upstream end roughly aligns with where Milillo et al. (2019) document the formation of an approximately 1 km wide subglacial channel near Cavities 1, 1a, and 2 (points C and D from Fig. 1 in Milillo et al. (2019)) before the grounding line retreated to its 2017 extent. They observed no change in velocity along the subglacial channel, and thus attribute thinning in this region to ocean melting rather than dynamic

570   thinning (Milillo et al., 2019; Millgate et al., 2013). Schmidt et al. (2023) confirmed strong basal melting in this region, with the fastest rates along the steep slopes of terraces at the ice–shelf base, consistent with observations at Pine Island Glacier (Dutrieux et al., 2014). Although Schmidt et al. (2023) did not sample at the location of ThC1, their finding that the greatest melting occurs along steep basal slopes in this region provides further evidence that ThC1 is a subglacially–sourced channel whose steep sides promote high melt rates and retreat along its trunk.

575   Two channels mapped by Alley et al. (2016) roughly align with the locations of ThC3 and ThC4, and a third runs parallel to the end of ThC7 but begins further downstream (Fig. S10). Alley et al. (2016) considered the basal channels parallel to ThC4 and ThC7 to be subglacially sourced. Our observations support this claim for ThC7 but suggest that ThC4 may be a grounding–line sourced incision as ice flows over local bedrock topographic highs as described in Sections 4.2.2 (Fig. 5), although we cannot confirm whether it entrains buoyant plumes. Furthermore, the retreat along SD3 also appears to be

580   coincident with a subglacial drainage channel modelled and mapped by Hager et al. (2022, Figure 5), although due to the breakdown of the hydrostatic assumption in the TWIT, we cannot confirm whether this inferred subglacial channel forms a basal channel in the ice shelf.

6 Conclusions

This study presents novel, time–evolving rates of ice–shelf thickness and basal mass change and proxies for grounding line
585   and basal channel position on the TGIS derived from high resolution REMA DSM products, providing further evidence linking
high basal melt rates along ice–shelf basal channels to rapid rates of grounding–zone retreat (e.g. Narkevic et al., 2023; Holland
et al., 2023; Ciracì et al., 2023). Hydrostatic boundary retreat rates averaging 0.6 km a^{-1} and at times > 3 km a^{-1} were observed
concurrently with persistent basal channels and melt rates as high as 250 m a^{-1}. The retreat is not fully attributable to the
presence of basal channels, as several regions where HB retreated along reference channels also had deep retrograde bed slopes
590   and/or were likely to be in contact with warm CDW. This study does not deconvolve all potential causes and effects of HB
retreat, such as changes in ice velocity through time (e.g. dos Santos et al., 2021), varying subglacial discharge (e.g. Hager et
al., 2022), or changing ocean currents (e.g. Holland et al., 2023; Dotto et al., 2022), but supports the hypothesis that basal
channels, whether initiated at the GZ or subglacially, are associated with more rapid GZ retreat than non–channelized areas.
Our observations are consistent with other work that suggests buoyant meltwater plumes can entrain CDW to form plumes
595   with strong melt (e.g. Le Brocq et al., 2013).

These results also provide additional evidence for the recent opening of new ice–shelf cavities not associated with
basal channels, as observed by Milillo et al. (2019), Bevan et al. (2021), and Schmidt et al. (2023), and point to the potential
for continued, unstable retreat of the grounding line (e.g. Yu et al., 2018; Joughin et al., 2014), particularly along inferred
subglacial drainage pathways. As the GZ continues to retreat and subglacial pressures change, we suggest that retreat along
600   existing and/or rerouted subglacial channels that intersect the GZ will continue to form narrow, Type 2 cavities in the future,
complicating the task of accurately predicting future GZ retreat.

Milillo et al. (2019) point out that several of the newly opened ice–shelf cavities have less than 100 m between the
ice–shelf base and the sea floor, and to simulate these melt and retreat processes would require a significantly finer spatial
resolution than is currently available to ocean models. This methodology can be applied to other ice shelves to further
605   investigate the prevalence of HB retreat at channelized and non–channelized grounding zones to further investigate relevant
changes in ice–shelf structure, velocity, melt rates, and subglacial drainage. This study is an important step towards better
understanding these complex and critical regions of the Antarctic ice sheet and the relevant temporal and spatial scales over
which these processes occur.

Code and Data Availability

610   REMA v4.1 2 m strips (DOI:10.7910/DVN/X7NDNY) and 200 m mosaics (DOI: 10.7910/DVN/EBW8UC) are available at
the Polar Geospatial Center. The following datasets are available at NSIDC DAAC: BedMachine Antarctica V003 bed heights,
firn and ice thicknesses, Eigen–6C4 geoid data (DOI: 10.5067/FPSU0V1MWUB6), MEaSURES Antarctic Boundaries for
IPY 2007–2009 from Satellite Radar V002 (DOI: 10.5067/AXE4121732AD), MEaSUREs Antarctic Grounding Line from
Differential Satellite Radar Interferometry V002 (DOI: 10.5067/IKBWW4RYHF1Q), MeASUREs InSAR–Based Antarctica

Ice Velocity Map V002 (DOI: 10.5067/D7GK8F5J8M8R), MEaSUREs Annual Antarctic Ice Velocity Maps V001 (DOI: 10.5067/9T4EPQXTJYW9), ATLAS/ICESat–2 L3A Land Ice Height V005 (DOI: 10.5067/ATLAS/ATL06.005) and V006 (DOI: 10.5067/ATLAS/ATL06.006), IceBridge MCoRDS L2 Ice Thickness V001 (DOI: 10.5067/GDQ0CUCVTE2Q), IceBridge ATM L1B Elevation and Return Strength V002 (DOI: 10.5067/19SIM5TXKPGT), IceBridge LVIS–GH L2 Geolocated Surface Elevation Product V001 (DOI: 10.5067/RELPCEXB0MY3), and IceBridge Riegl Laser Altimeter L2 Geolocated Surface Elevation Triplets V001 (DOI: 10.5067/JV9DENETK13E). The DTU22 MDT model is available at (2019). The CATS2008b tide model (DOI: 10.15784/601235) is available at USAP–DC. RACMO 3p2 data are available at https://www.projects.science.uu.nl/iceclimate/publications/data/2018/vwessem2018_tc/RACMO_Yearly/. TopoToolbox v2.3.1 is available on the Mathworks File Exchange.

All code, gridded products generated in this study (annual mosaics, annual velocities derived from the Amundsen Sea quarterly velocities, and rates of change), and shapefiles of the reference channels and annual HBs will be made freely available with a permanent DOI at Zenodo by the time of final publication. In the interim, near-final versions are available at DOI: 10.5281/zenodo.10969572.

Author Contributions

AC conceived the ideas and carried out analyses with support from IH. IH created the annual REMA DSM mosaics, IJ provided the quarterly velocity maps for the Amundsen Sea regions, and BS performed the CryoSat–2 registrations for the REMA DSM strips. AC prepared the manuscript with contributions from all authors.

Competing Interests

Some authors are members of the editorial board of The Cryosphere.

Acknowledgements

Allison Chartrand and Ian Howat were funded by the National Aeronautics and Space Administration (NASA: 80NSSC20K1658), the National Science Foundation (NSF: Award No. 2217574), and the Ohio State University. Ian Joughin was funded by NASA Grant 80NSSC20K0954.

References

Adusumilli, S., Fricker, H. A., Medley, B., Padman, L., and Siegfried, M. R.: Interannual variations in meltwater input to the Southern Ocean from Antarctic ice shelves, Nat. Geosci., 13, 616–620, https://doi.org/10.1038/s41561-020-0616-z, 2020.

Alley, K. E., Scambos, T. A., Siegfried, M. R., and Fricker, H. A.: Impacts of warm water on Antarctic ice shelf stability through basal channel formation, Nature Geosci, 9, 290–293, https://doi.org/10.1038/ngeo2675, 2016.

645 Alley, K. E., Scambos, T. A., Alley, R. B., and Holschuh, N.: Troughs developed in ice-stream shear margins precondition ice shelves for ocean-driven breakup, Science Advances, 5, eaax2215, https://doi.org/10.1126/sciadv.aax2215, 2019.

Bevan, S. L., Luckman, A. J., Benn, D. I., Adusumilli, S., and Crawford, A.: Brief communication: Thwaites Glacier cavity evolution, The Cryosphere, 15, 3317–3328, https://doi.org/10.5194/tc-15-3317-2021, 2021.

Blair, J. B. and Hofton, M.: IceBridge LVIS-GH L2 Geolocated Surface Elevation Product, Version 1, https://doi.org/10.5067/RELPCEXB0MY3, 2015.

650 Blankenship, D. D., Kempf, S., Young, D. A., Roberts, J. L., van Ommen, T., Forsberg, R., Siegert, M., Palmer, S. J., and Dowdeswell, J. A.: IceBridge Riegl Laser Altimeter L2 Geolocated Surface Elevation Triplets, Version 1, https://doi.org/10.5067/JV9DENETK13E, 2012.

Chartrand, A. M. and Howat, I. M.: Basal Channel Evolution on the Getz Ice Shelf, West Antarctica, J. Geophys. Res. Earth Surf., 125, https://doi.org/10.1029/2019JF005293, 2020.

655 Chartrand, A. M. and Howat, I. M.: A comparison of contemporaneous airborne altimetry and ice-thickness measurements of Antarctic ice shelves, Journal of Glaciology, 1–14, https://doi.org/10.1017/jog.2023.49, 2023.

Ciracì, E., Rignot, E., Scheuchl, B., Tolpekin, V., Wollersheim, M., An, L., Milillo, P., Bueso-Bello, J.-L., Rizzoli, P., and Dini, L.: Melt rates in the kilometer-size grounding zone of Petermann Glacier, Greenland, before and during a retreat, Proceedings of the National Academy of Sciences, 120, e2220924120, https://doi.org/10.1073/pnas.2220924120, 660 2023.

Dotto, T. S., Heywood, K. J., Hall, R. A., Scambos, T. A., Zheng, Y., Nakayama, Y., Hyogo, S., Snow, T., Wåhlin, A. K., Wild, C., Truffer, M., Muto, A., Alley, K. E., Boehme, L., Bortolotto, G. A., Tyler, S. W., and Pettit, E.: Ocean variability beneath Thwaites Eastern Ice Shelf driven by the Pine Island Bay Gyre strength, Nat Commun, 13, 7840, https://doi.org/10.1038/s41467-022-35499-5, 2022.

665 Dow, C. F., Lee, W. S., Greenbaum, J. S., Greene, C. A., Blankenship, D. D., Poinar, K., Forrest, A. L., Young, D. A., and Zappa, C. J.: Basal channels drive active surface hydrology and transverse ice shelf fracture, Science Advances, 4, eaao7212, https://doi.org/10.1126/sciadv.aao7212, 2018.

Drews, R.: Evolution of ice-shelf channels in Antarctic ice shelves, The Cryosphere, 9, 1169, https://doi.org/10.5194/tc-9-1169-2015, 2015.

670 Drews, R., Pattyn, F., Hewitt, I. J., Ng, F. S. L., Berger, S., Matsuoka, K., Helm, V., Bergeot, N., Favier, L., and Neckel, N.: Actively evolving subglacial conduits and eskers initiate ice shelf channels at an Antarctic grounding line, Nature Communications, 8, 1–10, https://doi.org/10.1038/ncomms15228, 2017.

Dutrieux, P., De Rydt, J., Jenkins, A., Holland, P. R., Ha, H. K., Lee, S. H., Steig, E. J., Ding, Q., Abrahamsen, E. P., and Schröder, M.: Strong Sensitivity of Pine Island Ice-Shelf Melting to Climatic Variability, Science, 343, 174–178, 675 https://doi.org/10.1126/science.1244341, 2014.

European Space Agency: L1b NOP-IOP-GOP SAR, Version Baseline C., https://doi.org/10.5270/CR2-gsyvnx0, 2023.

Förste, C., Bruinsma, Sean. L., Abrikosov, O., Lemoine, J.-M., Marty, J. C., Flechtner, F., Balmino, G., Barthelmes, F., and Biancale, R.: EIGEN-6C4 The latest combined global gravity field model including GOCE data up to degree and order 2190 of GFZ Potsdam and GRGS Toulouse, https://doi.org/10.5880/ICGEM.2015.1, 2014.

680 Gadi, R., Rignot, E., and Menemenlis, D.: Modeling Ice Melt Rates From Seawater Intrusions in the Grounding Zone of Petermann Gletscher, Greenland, Geophysical Research Letters, 50, e2023GL105869, https://doi.org/10.1029/2023GL105869, 2023.

Gillet-Chaulet, F., Durand, G., Gagliardini, O., Mosbeux, C., Mouginot, J., Rémy, F., and Ritz, C.: Assimilation of surface velocities acquired between 1996 and 2010 to constrain the form of the basal friction law under Pine Island Glacier, 685 Geophysical Research Letters, 43, 10,311-10,321, https://doi.org/10.1002/2016GL069937, 2016.

Goldberg, D. N., Heimbach, P., Joughin, I., and Smith, B.: Committed retreat of Smith, Pope, and Kohler Glaciers over the next 30 years inferred by transient model calibration, The Cryosphere, 9, 2429–2446, https://doi.org/10.5194/tc-9-2429-2015, 2015.

Gourmelen, N., Goldberg, D. N., Snow, K., Henley, S. F., Bingham, R. G., Kimura, S., Hogg, A. E., Shepherd, A., Mouginot, 690 J., Lenaerts, J. T. M., Ligtenberg, S. R. M., and Berg, W. J. van de: Channelized Melting Drives Thinning Under a

Rapidly Melting Antarctic Ice Shelf, Geophysical Research Letters, 44, 9796–9804, https://doi.org/10.1002/2017GL074929, 2017.

Gudmundsson, G. H., Krug, J., Durand, G., Favier, L., and Gagliardini, O.: The stability of grounding lines on retrograde slopes, The Cryosphere, 6, 1497–1505, https://doi.org/10.5194/tc-6-1497-2012, 2012.

695 Hager, A. O., Hoffman, M. J., Price, S. F., and Schroeder, D. M.: Persistent, extensive channelized drainage modeled beneath Thwaites Glacier, West Antarctica, The Cryosphere, 16, 3575–3599, https://doi.org/10.5194/tc-16-3575-2022, 2022.

Hoffman, M. J., Asay-Davis, X., Price, S. F., Fyke, J., and Perego, M.: Effect of Subshelf Melt Variability on Sea Level Rise Contribution From Thwaites Glacier, Antarctica, Journal of Geophysical Research: Earth Surface, 124, e2019JF005155, https://doi.org/10.1029/2019JF005155, 2019.

700 Hogan, K. A., Larter, R. D., Graham, A. G. C., Arthern, R., Kirkham, J. D., Totten, R. L., Jordan, T. A., Clark, R., Fitzgerald, V., Wåhlin, A. K., Anderson, J. B., Hillenbrand, C.-D., Nitsche, F. O., Simkins, L., Smith, J. A., Gohl, K., Arndt, J. E., Hong, J., and Wellner, J.: Revealing the former bed of Thwaites Glacier using sea-floor bathymetry: implications for warm-water routing and bed controls on ice flow and buttressing, The Cryosphere, 14, 2883–2908, https://doi.org/10.5194/tc-14-2883-2020, 2020.

705 Holland, P. R., Bevan, S. L., and Luckman, A. J.: Strong Ocean Melting Feedback During the Recent Retreat of Thwaites Glacier, Geophysical Research Letters, 50, e2023GL103088, https://doi.org/10.1029/2023GL103088, 2023.

Howat, I. M., Porter, C., Smith, B. E., Noh, M.-J., and Morin, P.: The Reference Elevation Model of Antarctica, The Cryosphere, 13, 665–674, https://doi.org/10.5194/tc-13-665-2019, 2019.

Jenkins, A.: Convection-Driven Melting near the Grounding Lines of Ice Shelves and Tidewater Glaciers, J. Phys. Oceanogr., 710 41, 2279–2294, https://doi.org/10.1175/JPO-D-11-03.1, 2011.

Joughin, I., Tulaczyk, S., Bamber, J. L., Blankenship, D., Holt, J. W., Scambos, T., and Vaughan, D. G.: Basal conditions for Pine Island and Thwaites Glaciers, West Antarctica, determined using satellite and airborne data, Journal of Glaciology, 55, 245–257, https://doi.org/10.3189/002214309788608705, 2009.

Joughin, I., Smith, B. E., and Medley, B.: Marine Ice Sheet Collapse Potentially Under Way for the Thwaites Glacier Basin, 715 West Antarctica, Science, 344, 735–738, https://doi.org/10.1126/science.1249055, 2014.

Joughin, I., Smith, B. E., and Schoof, C. G.: Regularized Coulomb Friction Laws for Ice Sheet Sliding: Application to Pine Island Glacier, Antarctica, Geophysical Research Letters, 46, 4764–4771, https://doi.org/10.1029/2019GL082526, 2019.

Joughin, I., Shapero, D., and Dutrieux, P.: Responses of Pine Island and Thwaites Glaciers to Melt and Sliding 720 Parameterizations, EGUsphere, 1–34, https://doi.org/10.5194/egusphere-2023-2929, 2024.

Knudsen, P., Andersen, O., and Maximenko, N.: A new ocean mean dynamic topography model, derived from a combination of gravity, altimetry and drifter velocity data, Advances in Space Research, 68, 1090–1102, https://doi.org/10.1016/j.asr.2019.12.001, 2021.

Le Brocq, A. M., Ross, N., Griggs, J. A., Bingham, R. G., Corr, H. F. J., Ferraccioli, F., Jenkins, A., Jordan, T. A., Payne, A. 725 J., Rippin, D. M., and Siegert, M. J.: Evidence from ice shelves for channelized meltwater flow beneath the Antarctic Ice Sheet, Nature Geoscience, 6, 945–948, https://doi.org/10.1038/ngeo1977, 2013.

Ligtenberg, S. R. M., Helsen, M. M., and Broeke, M. R. van den: An improved semi-empirical model for the densification of Antarctic firn, The Cryosphere, 5, 809–819, https://doi.org/10.5194/tc-5-809-2011, 2011.

Milillo, P., Rignot, E., Rizzoli, P., Scheuchl, B., Mouginot, J., Bueso-Bello, J., and Prats-Iraola, P.: Heterogeneous retreat and 730 ice melt of Thwaites Glacier, West Antarctica, Science Advances, 5, eaau3433, https://doi.org/10.1126/sciadv.aau3433, 2019.

Millgate, T., Holland, P. R., Jenkins, A., and Johnson, H. L.: The effect of basal channels on oceanic ice-shelf melting, Journal of Geophysical Research: Oceans, 118, 6951–6964, https://doi.org/10.1002/2013JC009402, 2013.

Morlighem, M.: MEaSUREs BedMachine Antarctica, Version 3, 2022.

735 Morlighem, M., Rignot, E., Binder, T., Blankenship, D., Drews, R., Eagles, G., Eisen, O., Ferraccioli, F., Forsberg, R., Fretwell, P., Goel, V., Greenbaum, J. S., Gudmundsson, H., Guo, J., Helm, V., Hofstede, C., Howat, I., Humbert, A., Jokat, W., Karlsson, N. B., Lee, W. S., Matsuoka, K., Millan, R., Mouginot, J., Paden, J., Pattyn, F., Roberts, J., Rosier, S., Ruppel, A., Seroussi, H., Smith, E. C., Steinhage, D., Sun, B., Broeke, M. R. van den, Ommen, T. D. van, Wessem, M. van, and Young, D. A.: Deep glacial troughs and stabilizing ridges unveiled beneath the margins of the 740 Antarctic ice sheet, Nature Geoscience, 13, 132–137, https://doi.org/10.1038/s41561-019-0510-8, 2020.

Mouginot, J., Scheuchl, B., and Rignot, E.: Mapping of Ice Motion in Antarctica Using Synthetic-Aperture Radar Data, Remote Sensing, 4, 2753–2767, https://doi.org/10.3390/rs4092753, 2012.

Mouginot, J., Scheuchl, B., and Rignot, E.: MEaSUREs Annual Antarctic Ice Velocity Maps 2005-2017, Version 1, , Boulder, Colorado USA, 2017a.

745   Mouginot, J., Scheuchl, B., and Rignot, E.: MEaSUREs Antarctic Boundaries for IPY 2007-2009 from Satellite Radar, Version 2, https://doi.org/10.5067/AXE4121732AD, 2017b.

Nakayama, Y., Menemenlis, D., Zhang, H., Schodlok, M., and Rignot, E.: Origin of Circumpolar Deep Water intruding onto the Amundsen and Bellingshausen Sea continental shelves, Nature Communications, 9, 3403, https://doi.org/10.1038/s41467-018-05813-1, 2018.

750   Narkevic, A., Csatho, B., and Schenk, T.: Rapid Basal Channel Growth Beneath Greenland's Longest Floating Ice Shelf, Geophysical Research Letters, 50, e2023GL103226, https://doi.org/10.1029/2023GL103226, 2023.

Nuth, C. and Kääb, A.: Co-registration and bias corrections of satellite elevation data sets for quantifying glacier thickness change, The Cryosphere, 5, 271–290, https://doi.org/10.5194/tc-5-271-2011, 2011.

Paden, J. D., Li, J., Leuschen, C., Rodriguez-Morales, F., and Hale, R.: IceBridge MCoRDS L2 Ice Thickness, Version 1, ,
755   Boulder, Colorado USA, 2010.

Paden, J. D., Li, J., Leuschen, Carl, Rodriguez-Morales, F., and Hale, R.: Pre-IceBridge MCoRDS L2 Ice Thickness, Version 1, , Boulder, Colorado USA, 2011.

Padman, L., Siegfried, M. R., and Fricker, H. A.: Ocean Tide Influences on the Antarctic and Greenland Ice Sheets, Rev. Geophys., 2016RG000546, https://doi.org/10.1002/2016RG000546, 2018.

760   Rignot, E., Mouginot, J., and Scheuchl, B.: Ice Flow of the Antarctic Ice Sheet, Science, 333, 1427–1430, https://doi.org/10.1126/science.1208336, 2011.

Rignot, E., Mouginot, J., Morlighem, M., Seroussi, H., and Scheuchl, B.: Widespread, rapid grounding line retreat of Pine Island, Thwaites, Smith, and Kohler glaciers, West Antarctica, from 1992 to 2011, Geophysical Research Letters, 41, 3502–3509, https://doi.org/10.1002/2014GL060140, 2014.

765   Rignot, E., Mouginot, J., and Scheuchl, B.: MEaSUREs Antarctic Grounding Line from Differential Satellite Radar Interferometry, Version 2, https://doi.org/10.5067/IKBWW4RYHF1Q, 2016.

Rignot, E., Mouginot, J., and Scheuchl, B.: MEaSUREs InSAR-Based Antarctica Ice Velocity Map, Version 2, https://doi.org/10.5067/D7GK8F5J8M8R, 2017.

Rignot, E., Mouginot, J., Scheuchl, B., van den Broeke, M., van Wessem, M. J., and Morlighem, M.: Four decades of Antarctic
770   Ice Sheet mass balance from 1979–2017, Proceedings of the National Academy of Sciences, 116, 1095–1103, https://doi.org/10.1073/pnas.1812883116, 2019.

dos Santos, T. D., Barnes, J. M., Goldberg, D. N., Gudmundsson, G. H., and Morlighem, M.: Drivers of Change of Thwaites Glacier, West Antarctica, Between 1995 and 2015, Geophysical Research Letters, 48, e2021GL093102, https://doi.org/10.1029/2021GL093102, 2021.

775   Schmidt, B. E., Washam, P., Davis, P. E. D., Nicholls, K. W., Holland, D. M., Lawrence, J. D., Riverman, K. L., Smith, J. A., Spears, A., Dichek, D. J. G., Mullen, A. D., Clyne, E., Yeager, B., Anker, P., Meister, M. R., Hurwitz, B. C., Quartini, E. S., Bryson, F. E., Basinski-Ferris, A., Thomas, C., Wake, J., Vaughan, D. G., Anandakrishnan, S., Rignot, E., Paden, J., and Makinson, K.: Heterogeneous melting near the Thwaites Glacier grounding line, Nature, 614, 471–478, https://doi.org/10.1038/s41586-022-05691-0, 2023.

780   Schoof, C.: Ice sheet grounding line dynamics: Steady states, stability, and hysteresis, J. Geophys. Res., 112, F03S28, https://doi.org/10.1029/2006JF000664, 2007.

TopoToolbox: https://www.mathworks.com/matlabcentral/fileexchange/50124-topotoolbox, last access: 21 June 2023.

Seroussi, H., Nakayama, Y., Larour, E., Menemenlis, D., Morlighem, M., Rignot, E., and Khazendar, A.: Continued retreat of Thwaites Glacier, West Antarctica, controlled by bed topography and ocean circulation, Geophysical Research
785   Letters, 44, 6191–6199, https://doi.org/10.1002/2017GL072910, 2017.

Shean, D. E., Joughin, I. R., Dutrieux, P., Smith, B. E., and Berthier, E.: Ice shelf basal melt rates from a high-resolution digital elevation model (DEM) record for Pine Island Glacier, Antarctica, The Cryosphere, 13, 2633–2656, https://doi.org/10.5194/tc-13-2633-2019, 2019.

Smith, B. E., Adusumilli, S., Csatho, B. M., Felikson, D., Fricker, H. A., Gardner, A. S., Holschuh, N., Lee, J., Nilsson, J., Paolo, F. S., Siegfried, M. R., Sutterley, T. C., and ICESat-2 Science Team: ATLAS/ICESat-2 L3A Land Ice Height, Version 5, https://doi.org/10.5067/ATLAS/ATL06.005, 2021.

Smith, B. E., Adusumilli, S., Csatho, B. M., Felikson, D., Fricker, H. A., Gardner, A. S., Holschuh, N., Lee, J., Nilsson, J., Paolo, F. S., Siegfried, M. R., Sutterley, T. C., and ICESat-2 Science Team: ATLAS/ICESat-2 L3A Land Ice Height, Version 6, https://doi.org/10.5067/ATLAS/ATL06.006, 2023.

Studinger, M.: IceBridge ATM L1B Elevation and Return Strength, Version 2, https://doi.org/10.5067/19SIM5TXKPGT, 2013.

Vaughan, D. G., Corr, H. F. J., Bindschadler, R. A., Dutrieux, P., Gudmundsson, G. H., Jenkins, A., Newman, T., Vornberger, P., and Wingham, D. J.: Subglacial melt channels and fracture in the floating part of Pine Island Glacier, Antarctica, J. Geophys. Res., 117, F03012, https://doi.org/10.1029/2012JF002360, 2012.

Washam, P., Nicholls, K. W., Münchow, A., and Padman, L.: Summer surface melt thins Petermann Gletscher Ice Shelf by enhancing channelized basal melt, Journal of Glaciology, 65, 662–674, https://doi.org/10.1017/jog.2019.43, 2019.

Wearing, M. G., Stevens, L. A., Dutrieux, P., and Kingslake, J.: Ice-Shelf Basal Melt Channels Stabilized by Secondary Flow, Geophysical Research Letters, 48, e2021GL094872, https://doi.org/10.1029/2021GL094872, 2021.

Weertman, J.: Stability of the Junction of an Ice Sheet and an Ice Shelf, Journal of Glaciology, 13, 3–11, https://doi.org/10.1017/S0022143000023327, 1974.

van Wessem, J. M., van de Berg, W. J., Noël, B. P. Y., van Meijgaard, E., Amory, C., Birnbaum, G., Jakobs, C. L., Krüger, K., Lenaerts, J. T. M., Lhermitte, S., Ligtenberg, S. R. M., Medley, B., Reijmer, C. H., van Tricht, K., Trusel, L. D., van Ulft, L. H., Wouters, B., Wuite, J., and van den Broeke, M. R.: Modelling the climate and surface mass balance of polar ice sheets using RACMO2 – Part 2: Antarctica (1979–2016), The Cryosphere, 12, 1479–1498, https://doi.org/10.5194/tc-12-1479-2018, 2018.

Wild, C. T., Alley, K. E., Muto, A., Truffer, M., Scambos, T. A., and Pettit, E. C.: Weakening of the pinning point buttressing Thwaites Glacier, West Antarctica, The Cryosphere, 16, 397–417, https://doi.org/10.5194/tc-16-397-2022, 2022.

Yu, H., Rignot, E., Seroussi, H., and Morlighem, M.: Retreat of Thwaites Glacier, West Antarctica, over the next 100 years using various ice flow models, ice shelf melt scenarios and basal friction laws, The Cryosphere, 12, 3861–3876, https://doi.org/10.5194/tc-12-3861-2018, 2018.

Zinck, A.-S. P., Wouters, B., Lambert, E., and Lhermitte, S.: REMA reveals spatial variability within the Dotson Melt Channel, The Cryosphere Discussions, 1–25, https://doi.org/10.5194/tc-2023-14, 2023.